FUNDAMENTAL ELECTRONIC AND STRUCTURAL PROPERTIES OF CARBON ONIONS IN EXTREME ENVIRONMENTS

By

Raied A. Al-Duhileb

A THESIS

Submitted to
Michigan State University
in partial fulfillment of the requirements
for the degree of

MASTER OF SCIENCE

Electrical Engineering

2010

ProQuest LLC
789 East Eisenhower Parkway
P.O. Box 1346
Ann Arbor, MI 48106-1346

ABSTRACT

FUNDAMENTAL ELECTRONIC AND STRUCTURAL PROPERTIES OF CARBON ONIONS IN EXTREME ENVIRONMENTS

By

Raied A. Al-Duhileb

The purpose of this research is to investigate the fundamental tribological (frictional) and stability characteristics of the fullerene-related nano-materials, carbon onions, which are nested fullerenes of typically 5-10 shells. Due to their distinctive structures, the frictional performance of carbon onions in different surroundings seems to be enhanced compared to those of other nano-materials. The objectives of this research are to: 1) investigate the nanoscopic structural properties of carbon onions using high resolution electron microscopy (HRTEM) including the known structural change from spherical to polygonal as a function of synthesis temperature; 2) investigate the change in the sp^2/sp^3 ratio as a function of increasing synthesis temperature using electron energy loss spectroscopy (EELS); 3) investigate their oxygen functionalities using Raman spectroscopy; 4) investigate their film stability using scanning electron microscopy (SEM); and 5) assess their tribological performance in different environments using a ball-on-disc tribometer.

The practical merit of this research is to develop an environmentally benign solid lubricant that can be widely used in various applications. Experimental results have shown that these nano-materials have unique structures and an increasing sp^2/sp^3 bond hybridization ratio as a function of increasing synthesis temperature.

To my parents and lovely wife,

who provided all the support

to make it becomes true

TABLE OF CONTENTS

List of Tables ..... **vi**

List of Figures ..... **vii**

1 Introduction **1**
1.1 Literature Review of Carbon Nano-Materials 3
1.1.1 Carbon Onions 5
1.1.2 C_{60} Fullerenes (Buckyballs) 10
1.1.3 Nanocrystalline Diamond (NCD) 13

2 Characterization Instruments and Methods **21**
2.1 Transmission Electron Microscopy 21
2.1.1 TEM Operation 24
2.2 Scanning Electron Microscopy 27
2.3 Electron Energy Loss Spectroscopy 30
2.4 Raman Spectroscopy 35
2.5 Sample Preparation Methods 37
2.5.1 TEM, SEM, and EELS Samples 37

3 Carbon Atom Hybridization **40**
3.1 Hybrid Orbital Introduction 40
3.2 sp Hybrid Orbitals 41
3.3 sp^2 Hybrid Orbitals 44
3.4 sp^3 Hybrid Orbitals 46

4 Quantitative EELS Investigation of Carbon Materials **50**
4.1 Quantitative Method: EELS 51
4.2 Quantitative EELS: Research Issues 52
4.2.1 Near-Edge Segregation 52
4.2.2 sp^2 Reference Samples 54
4.2.3 Inclusion of the 287.0 eV Peak 56
4.3 EELS Deconvolution Techniques 56
4.3.1 Two-Energy Windows Method 56
4.3.2 Functional Fitting Method 56

5 Quantitative EELS Investigation of Carbon Onions **60**

5.1 Structural Characterization Using HRTEM 60
5.2 EELS Deconvolution: Gaussian Function 64
5.3 EELS Deconvolution: Lorentzian Function 68
5.4 EELS Deconvolution: F-Variance Function 72
5.4.1 Investigation of Synthesis Uniformity by SEM 77

6 Conclusion and Future Work 79
6.1 Discussed Research Conclusion 79
6.2 Continuing Fundamental Studies: Raman Spectroscopy 80
6.3 Continuing Application Studies: Irradiated Carbon Onions 82
6.4 Continuing Application Studies: Tribological Performance of Carbon Onions in Harsh Environments 87

LIST OF TABLES

Table 1.1 Physical properties of C_{60} fullerenes (Buckyballs). (Table: adapted from Hirata *et al.* [3], and www.sesres.com/PhysicalProperties.asp [34]) 10

Table 5.1 sp^2/sp^3 ratio of carbon onion samples prepared at increasing synthesis temperature. The results were obtained using Gaussian deconvolution and 2-peak fit.... 65

Table 5.2 sp^2/sp^3 ratio of carbon onion samples prepared at increasing synthesis temperature. The results were obtained using Gaussian deconvolution and 3-peak fit.... 67

Table 5.3 sp^2/sp^3 ratio of carbon onion samples prepared at increasing synthesis temperature. The results were obtained using symmetric Lorentzian area deconvolution with 3-peak fit and fixed starting & end points 69

Table 5.4 First and second inflection points (IPs) and their corresponding differences. 71

Table 5.5 First sp^2/sp^3 ratio of carbon onion samples prepared at increasing synthesis temperature. The results were obtained using symmetric Lorentzian area deconvolution with 3-peak fit and exact inflection points..... 72

Table 5.6 sp^2/sp^3 ratio of carbon onion samples prepared at increasing synthesis temperature. The results were obtained using asymmetric f-variance area deconvolution and 2-peak fit 75

Table 6.1 Raman spectroscopy of C_{60} and Carbon Onions at wavelength 532 nm 82

LIST OF FIGURES

Figure 1.1 An HRTEM image showing the multi-layer structure of carbon onions. (Image: Raied A. Al-Duhileb) 6

Figure 1.2 EELS core loss spectra of (a) NCD, (b) spherical carbon onions, and (c) polyhedral carbon onions. (Image: adapted from Tomita *et al.* [22]) 8

Figure 1.3 Raman spectra of carbon onion samples prepared at increasing synthesis temperature. (Image: adapted from Tomita *et al.* [20]) 9

Figure 1.4 An HRTEM image of a single-walled carbon nanotube filled with a linear chain of C_{60} particles. (Image: Benjamin W. Jacobs) 12

Figure 1.5 Raman spectra of a film of purified C_{60}. (Image: adapted from Bethune *et al.* [39]) 13

Figure 1.6 An HRTEM HRTEM image of NCD particles having an average size of 5 nm. (Image: Raied A. Al-Duhileb) 14

Figure 1.7 EELS core loss spectra of purified NCD particles. Results revealed a single peak at 289 eV and were free of sp^2 bonded carbon. (Image: adapted from Hansen *et al.* [36]) 15

Figure 1.8 A Raman spectrum of NCD. (Image: adapted from Hansen *et al.* [36]) 16

Figure 2.1 The TEM anatomy. The thermionic or field emission electron gun emits a beam of focused electrons that penetrate the thin sample. The magnetic condenser, objective, diffraction, intermediate, and projector lenses control the electron beam and bring it to a focal point. Electrons that pass the sample are collected and the image is shown on the viewing screen or camera. (Image: Raied A. Al-Duhileb) 23

Figure 2.2 Typical diffraction pattern (single crystal pattern). (Image: Raied A. Al-Duhileb) 25

Figure 2.3 Determining the atomic lattice spacing (d) in diffraction mode using wave length of the electron (λ), camera length (L), and relative distance between the diffraction spots (R). (Image: Raied A. Al-Duhileb) 26

Figure 2.4 A schematic diagram illustrating the basic components and operation of an SEM. An electron gun focuses an electron beam on the surface of the sample. This results in producing secondary electrons that are collected by special electron detector and displayed as a mapped image on a screen. (Image: adapted from www.chm.bris.ac.uk [3]) 28

Figure 2.5 Energy level diagram showing excitation from the inner shell (valance band) into the empty state higher shell. (Image: adapted from Brundle *et al.* [1]) 31

Figure 2.6 The magnetic prism is used to record the intensity of scattered electrons at different position to obtain the energy loss spectrum. (Image: Raied A. Al-Duhileb) 31

Figure 2.7 A schematic diagram illustrating the shape of the inner-shell ionization edge of an element in the periodic table. (Image: Raied A. Al-Duhileb) 32

Figure 2.8 Excitation of an inner-shell electron by incident light beam photons. The energy of the scattered light beam photons is less than the energy of the incident laser beam photons. (Image: Raied A. Al-Duhileb) 36

Figure 2.9 A schematic Raman scattering spectrum showing Rayleigh line, Stokes scattering, and anti-Stokes scattering. (Image: adapted from Denk [7]) 37

Figure 3.1 A hybridization model of sp orbitals. An electron is promoted to a higher empty state due to the small energy differences between the lower 2s and the upper 2p energy levels. (Image: Raied A. Al-Duhileb) 42

Figure 3.2 New atomic orbitals (i.e. sp_a and sp_b) resulting from mixing the 2s orbital with one of the 2p orbitals ($2p_x$, $2p_y$, or $2p_z$). The resulting energy states are located in opposite directions, and centered on the atom. (Image: adapted from www.chem.umass.edu [5]) 43

Figure 3.3 A hybridization model of sp^2 orbitals. (Image: Raied A. Al-Duhileb) 45

Figure 3.4 New atomic orbitals (i.e., sp^2_a, sp^2_b, and sp^2_c) resulting from mixing the 2s orbital with two of the 2p orbitals ($2p_x$, $2p_y$, or $2p_z$). (Image: adapted from www.chem.umass.edu [5]) 46

Figure 3.5 A hybridization model of sp^3 orbitals. (Image: Raied A. Al-Duhileb)..... 47

Figure 3.6 New atomic orbitals (i.e., sp^3_a, sp^3_b, sp^3_c, and sp^3_d) resulting from mixing the 2s orbital with the three 2p orbitals ($2p_x$, $2p_y$, and $2p_z$). (Image: adapted from www.chem.umass.edu [5]) 47

Figure 4.1 A typical EELS spectrum from a largely sp^2 carbon sample with the transition edges marked 52

Figure 4.2 A theoretical calculation of the energy-loss-near-edge structure (ELNES) for a purely sp^2 graphite..... 53

Figure 5.1 An HRTEM image of the largely sp^3 NCD. (Image: Raied A. Al-Duhileb). 61

Figure 5.2 HRTEM images of the structural transition from spherical to polygonal for carbon onions synthesized at temperatures (a) 1700°C (b) 2000°C and (c) 2300°C. (Image: Raied A. Al-Duhileb) 62

Figure 5.3 A TEM image showing aggregate C_{60} particles suspended over a lacey film hole. (Image: Raied A. Al-Duhileb) 63

Figure 5.4 Deconvolution of the core loss EELS spectrum of carbon onions, prepared at 1700°C. The original spectrum was deconvolved using 2-peak fit and the symmetric Gaussian deconvolution. (Image: produced using the OriginPro software package)..... 65

Figure 5.5 A plot of the sp^2/sp^3 ratio in carbon onions as a function of synthesis temperature. The plot is based on results obtained using 2-peak fit and the symmetric Gaussian deconvolution. (Image: produced using the OriginPro software package)..... 66

Figure 5.6 Deconvolution of the core loss EELS spectrum of carbon onions, prepared at 1700°C. The original spectrum was deconvolved using 3-peak fit and the symmetric Gaussian deconvolution. (Image: produced using the OriginPro software package)..... 67

Figure 5.7 A plot of the sp^2/sp^3 ratio in carbon onions as a function of synthesis temperature. The plot is based on results obtained using 3-peak fit and the symmetric Gaussian deconvolution. (Image: produced using the OriginPro software package)..... 68

Figure 5.8 Deconvolution of the core loss EELS spectrum of carbon onions, prepared at 1700°C. The original spectrum was deconvolved using 3-peak fit and the symmetric Lorentzian area deconvolutio. (Image: produced using the OriginPro software package)70

Figure 5.9 A plot of the sp^2/sp^3 ratio in carbon onions as a function of synthesis temperature. The plot is based on results obtained using approach. (Image: produced using the OriginPro software package)..... 70

Figure 5.10 A plot of the sp^2/sp^3 ratio in carbon onions as a function of synthesis temperature. The plot is based on results obtained using approach 2. (Image: produced using the OriginPro software package)..... 72

Figure 5.11 Theoretical near edge π^* and σ^* spectra from an orientation resolved calculation, in which a graphite sample and the electron beam were at the "magic angle" 74

Figure 5.12 Deconvolution of the core loss EELS spectrum of carbon onions, prepared at 1700°C. The original spectrum was deconvolved using 2-peak fit and the asymmetric f-variance function. (Image: produced using the OriginPro software package)..... 76

Figure 5.13 A plot showing an increase in the sp^2/sp^3 ratio in carbon onions as a function of synthesis temperature. The results from the 2000°C were variable due to synthesis uniformity issues. (Image: produced using the OriginPro software package).. 76

Figure 5.14 SEM surface images of carbon onions synthesized at temperatures (a) 1700°C (b) 2000°C and (c) 2300°C. Images by: Raied A. Al-Duhileb..... 77

Figure 6.1 Experimental Raman spectra of C_{60} and carbon onion samples prepared at increasing synthesis temperature. (Image: produced using the OriginPro software package) 81

Figure 6.2 HRTEM images of pre-radiation carbon onion samples prepared at1700°C. Typical spherical morphologies are observed in (a). A fused onions feature is observed in (b). (Images by: Xudong Fan, with Kaylee McElroy, and Virginia M. Ayres)..... 84

Figure 6.3 HRTEM images of carbon onion samples prepared at 1700°C following irradiation with fully stripped Calcium-48 heavy ions at energies (a-c) 70 MeV/nucleon and (d-e) 140 MeV/nucleon. (Images by: Xudong Fan, with Kaylee McElroy, and Virginia M. Ayres)..... 86

Chapter 1

Introduction

Current conventional lubricants that are introduced between moving surfaces to reduce frictional forces and improve efficiency of machinery applications are often exposed to extreme environments. The performance of the existing lubricant approaches in severe environments like space, chemical, and petroleum mediums faces many challenges that might cause degradation and failure of these substances. For example, liquid lubricants require frequent maintenance in terrestrial industries, and are not practicable in space applications due to the exposure to vacuum.

To overcome the deficiencies of the presently available liquid lubricants, researchers in tribology (science of friction) have been examining solid-based lubricant alternatives[1,2,3]. Although graphite is the most familiar solid lubricant, experiments with graphite films have revealed friction coefficients of about 0.21 in air but only 0.5 to 0.6 in vacuum. The increase of the friction coefficient in vacuum is a well known effect due to the absence of assisting agents like water vapor and oxygen[4]. This is usually compensated by adding heavy metals, such as molybdenum or tungsten disulfide. These additives introduce an environmentally hazardous moiety that is not present in typical graphitic solid lubricants used in air[3].

Nano-materials such as carbon nanotubes (CNTs)[2], C_{60}, and carbon onions[3] are solid-based substances with new properties enabled by their nanoscopic size. Recent research indicates that nano-materials could exhibit better frictional performance in such

extreme environments compared to conventional materials[2,3]. Preliminary studies have shown that these materials have low (< 1.0) friction coefficients in air and vacuum, and maintain consistent behavior when exposed to heat and radiation[1,2,3]. Single-walled CNTs (SWCNTs) exhibit friction coefficients of (~0.6) in air and an improved tribological performance in vacuum (~0.2)[2]. C_{60} particles have friction coefficients of around 0.5 to 0.8 in both air and vacuum[3]. These results were due to infinitesimal size of these nano-materials, which tend to clump and compress into high shear strength layers[5]. Carbon onions, on the other hand, have shown the lowest friction coefficients of about 0.03 in both air and vacuum[3]. These nano-materials do not require potentially hazardous additives to attain their desirable tribological properties in vacuum; therefore, they show great promise as an environmentally benign solid lubricant in both ambient and vacuum environments[3].

Carbon onions, consisting of multiple layers of concentric graphitic shells, are fullerene-related nano-materials. Daniel Ugarte first observed them as a result of electron beam irradiation of soot or diamond clusters in high resolution transmission electron microscopy (HRTEM)[3,6,7]. They have been recognized as a new form of carbon with unique structure[3]; however, their fundamental properties have been far less studied than those of C_{60} and other single-layer fullerenes such as C_{70}. This research primarily focuses on investigating the tribological and stability characteristics of carbon onions in air and vacuum because they are expected to be effective and safe solid lubricant for many potential applications.

To fully exploit the great potential of carbon onions as a solid lubricant, one needs to study their physical structures, investigate their electronic structures and chemical composition, and assess their tribological performance in different environments.

In this research, the surfaces and internal structures of carbon onions prepared at increasing synthesis temperature are extensively studied using high resolution transmission electron microscopy (HRTEM). The integrated areas under the carbon K-ionization edges obtained using electron energy loss spectroscopy (EELS) are also quantified to precisely measure the change in the sp^2/sp^3 ratio. In addition, several state-of-the-art material characterization methodologies like Raman Spectroscopy are used to confirm the electronic structure of these nano-materials. C_{60} particles, which are pure sp^2 nano-materials, are used as a control to characterize the properties of carbon onions. Good quality nanocrystalline diamond (NCD) powders, which are nearly pure sp^3 nano-materials, are used as the starting material for preparing the carbon onion samples. Scanning electron microscopy (SEM) is used to assess carbon onion film stability on wear surfaces. These nanoscopic experimental results are then correlated with the macroscopic frictional performance of carbon onions assessed using a ball-on-disk tribometer.

1.1. Literature Review of Carbon Nano-Materials

For a long period of time, the element carbon has been thought to have three major solid forms or allotropes under ambient conditions: diamond, graphite and amorphous carbon. Its physical properties depend on its chemical bonding types.

Diamond, which has sp^3 hybridized bonds, is a transparent and hard material, whereas graphite, which has sp^2 hybridized bonds, is opaque and soft[8].

In 1985, a new form of carbon that was later called Buckminsterfullerene or Fullerenes was discovered by Kroto et al[9]. Due to their remarkable discovery of this new carbon allotrope, H. Kroto, R. Curl, and R. Smalley were awarded the 1996 Nobel Prize for Chemistry. This new carbon form may have several shapes such as hollow sphere or ellipsoid, and could contain both sp^3 and sp^2 bonding sites[10]. In 1991, research by S. Iijima extended the fullerene family to include single-walled and multi-walled CNTs[11]. The discovery of fullerenes has significantly increased the number of known carbon allotropes and resulted in starting a new era in science forming the beginning of nanotechnology.

Scientists have been investigating the properties of these fullerene-related nano-materials since their discovery. It has been found that the crystal size of these nano-materials in general is an important parameter that requires further consideration when studying their characteristics. The stability of nano-structures differs from that of bulk materials[12]. For instance, carbon clusters having less than 10^4 atoms were discovered to continue exhibiting liquid-like behavior at very low temperatures that are far below the melting point of the corresponding bulk materials, and are subject to surface reconstructions. However, C_{60}, and carbon nanotubes and their multi-shell versions are highly stable crystals of nano-scale size [13].

Although graphite is the most known stable form of carbon crystals having a lattice constant greater than 10 nm, it is believed that fullerene-related nano-materials are more stable and preferred form for tiny clusters having lattice constant less than 2 nm. It

was found that, as the crystal dimensions increase, the stability of the fullerene-related nano-materials decreases[14]. C_{60} fullerenes (also known as buckyballs) are the most stable fullerenes identified to date. These consist of 60 carbon atoms that are arranged in 20 hexagons and 12 pentagons, and have an average diameter of 1 nm. Carbon onions are composed of several concentric fullerene shells with a C_{60} inner shell. The outer shells would be individually less stable than C_{60} due to their larger sizes (~ 5-10 nm)[15]; however, the inter-layer interactions of the multi-shell carbon onion system provide an additional source of stability. Also, stability is affected by whether the individual shells are perfectly crystalline or defective. One critical parameter explored in this thesis is the defect concentration of the individual shells and how this affects the carbon onion properties.

Depending on the local energetic conditions, the small differences in the stability of fullerene-related nano-materials may cause phase transformations between different allotropes[16]. For instance, carbon onions can transform into other carbon forms such as (NCD) and vice versa[17,18]. They can also transform into other cage structures like CNTs, which are allotropes of carbon with a hollow cylindrical nanostructure[19].

1.1.1. Carbon Onions

Carbon onions are hollow nanometric fullerene-related materials that typically have 7 to 10 fullerene shells with outer diameters ranging from 5 to 10 nm as shown in Figure 1.1[20]. The largest carbon onion molecules, which were synthesized by Daniel Ugarte of the Federal Polytechnic School in Switzerland, have around 70 concentric fullerene shells[21]. These nano-materials can be produced in small quantities using several

methods such as heat treatment of amorphous carbon soot or NCD particles as in the present research, and ion implantation of carbon into metal substrates. The former preparation method has the advantage of producing carbon onions with uniform size and varied morphology[22]. Industrial scale-up of combustion methods with carefully controlled operation and gas mixture parameters is enabling commercial quantity production[23].

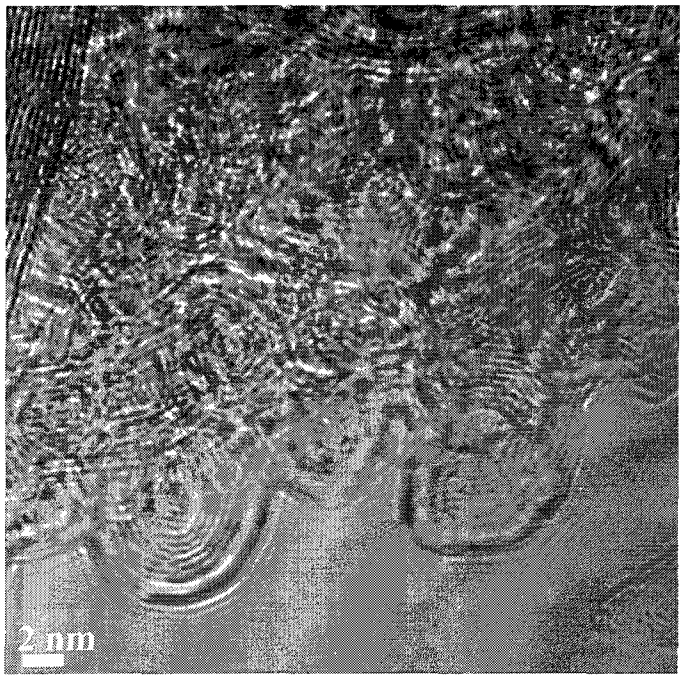

Figure 1.1 An HRTEM image showing the multi-layer structure of carbon onions. Image by: Raied A. Al-Duhileb.

The physical properties of these nano-materials strongly depend on the growth conditions. HRTEM images have shown a structural evolution from spherical to polyhedral multi-graphitic shells as the synthesis temperature is increased. This structural evolution has been associated with a change in the sp^2/sp^3 ratio, and assumed to be due to a reduction in the potential sp^3-defective hybridized bonds that are seen as broken shells under the HRTEM[24,25]. A contribution of this thesis is that the assumed correlation of

spherical to polyhedral multi-graphitic shells with a change in the sp^2/sp^3 ratio is quantitatively investigated using EELS. It is essential for the synthesis of optimum carbon onion lubricating particles to precisely determine the change in their sp^2/sp^3 ratio as the growth temperature increases. Researchers have been utilizing several approaches like HRTEM, EELS, and Raman Spectroscopy to investigate this phenomenon[3, 22]. We next review the results reported to date from each technique.

Early work by the Butenko group[26] identified the spherical to polyhedral evolution of the carbon onions as a function of the synthesis temperature. This result has since been established by several groups[20,25] including ours.

Early literature for EELS reported the core loss spectra (i.e. K-ionization edges) of spherical carbon onions prepared at lower annealing temperatures are slightly different from those of polyhedral carbon onions prepared at higher synthesis temperatures. EELS spectra of spherical carbon onions are more similar to NCD K-ionization edges, whereas those of polyhedral carbon onions show some dissimilarities as shown in Figure 1.2[22,24]. It was generally concluded that the similarity between spherical carbon onions and NCD spectrum is due to the presence of sp^3 bonds in both materials. Spherical carbon onions are believed to have such hybridized bonding because either they contain a small residual amount of diamond particles, or sp^3 bonds remain as structural defects at lower growth temperatures[22].

The tribological performance of carbon onions was also reported in the literature. These nano-materials reveal stable friction coefficients (< 0.1) both in air and vacuum[3]. It has been noticed that frictional performance of these nano-materials improves as the carbon onion size gets larger.

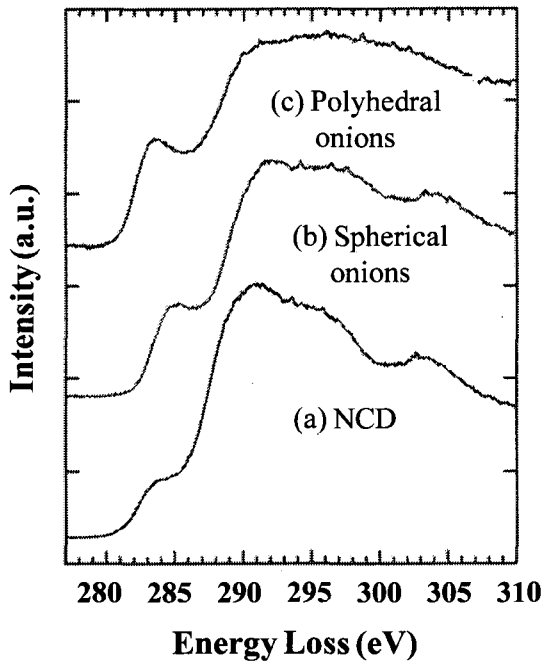

Figure 1.2 EELS core loss spectra of (a) NCD, (b) spherical carbon onions, and (c) polyhedral carbon onions[22].

Raman spectroscopy, which is widely utilized in material sciences to examine the phonon modes of different allotropes and carbon phases, has also been used to characterize the nano-structure of carbon onions[20]. Raman spectra of carbon onion samples, synthesized at different increasing temperatures, have revealed two broad Raman bands at about 1350 and 1580 cm^{-1} as shown in Figure 1.3. The former band at about 1350 cm^{-1} was identified as a *D* band or disorder band due to the presence of finite-sized graphite crystallites, dangling alkanes, etc. The second band at about 1580 cm^{-1} was reported as a *G* band. In planar graphite, the *G* peak at 1580 cm^{-1} corresponds to two very close modes, which are the stretch mode of a single graphene layer and the shear mode of two graphene layers. In Ref. [20], it was reported that the full width at half maximum (FWHM) of the *G* band decreased as the synthesis temperature increased.

The Ref. [20] results were acquired at room temperature, and are reminiscent of the differences between the Raman spectra of single-walled and multi-walled carbon nanotubes. Single-walled carbon nanotubes show clear peaks that correspond to identified breathing (A) and tangential (E) modes[27]. Multi-walled carbon nanotubes show two broad peaks that are very similar to those shown in Figure 1.3[28]. Similarly, the single-walled C_{60} Raman spectrum shows clear peaks that correspond to identified breathing and tangential (H and T) modes[29,30], while at room temperature, the multi-walled carbon onion Raman spectrum shows broad peaks. One of the contributions of this thesis is the first, as far as we know, low temperature (77K) Raman spectroscopy of multi-walled carbon onions, which is resolved into a series of clear peaks.

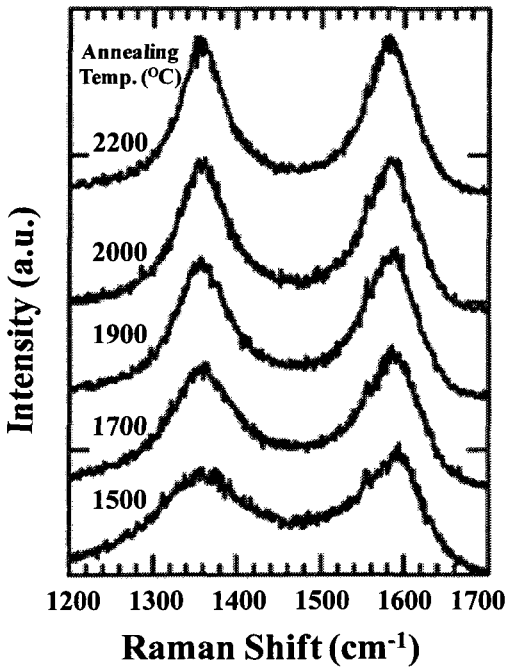

Figure 1.3 Raman spectra of carbon onion samples prepared at increasing synthesis temperature[20].

1.1.2. C_{60} Fullerenes (Buckyballs)

To characterize the properties of carbon onions, pure sp^2 C_{60} particles are used in this research as a control nano-material. Although C_{60}, which is the most stable form of fullerenes, was first produced in isolable quantities in 1990 by causing an arc between two graphite rods to burn in a helium atmosphere, some of its chemical and physical properties remain unclear, and are under investigation. It is known to consist of 20 hexagons and 12 pentagons that are the basis of a symmetrical closed cage structure. Each carbon atom is tied to three other carbon atoms, and is sp^2 hybridized[9]. C_{60} fullerenes have two bond lengths. The 6:6 ring bonds (~1.40 Å), which are double bonds, are shorter than the 6:5 bonds (~1.458 Å)[31]. They tend not to form double bonds in the pentagons, causing poor electron delocalization in these areas. Consequently, C_{60} molecules act as electron-deficient alkenes and react with electron-rich species[32]. Experiments have shown that C_{60} molecules are soluble in some solvents, such as benzene, toluene and chloroform[33]. Some physical properties of C_{60} are listed in Table 1.1.

Table 1.1 Physical properties of C_{60} fullerenes (Buckyballs)[34]

Average C-C distance	1.44 (Å)	**Resistivity**	1014 (ohm.m)
Average Friction Coefficient[3]	0.5	**Thermal conductivity**	0.4 (W/mK)
Density	1.72 ($g.cm^{-3}$)	**Boiling point**	Sublimes at 800 K

Several experiments aiming to investigate the electronic properties and chemical structures of C_{60} molecules have been carried out using different material characterization

methodologies, such as HRTEM and EELS. A group of C_{60} fullerenes at the edge of a lacey film hole cannot be resolved into individual cages, and conclusively identified due to their low contrast and small size (~1 nm diameter). Therefore, different methods were reported to view the structure of C_{60} molecules. One way, used in this thesis, is investigate a small-diameter carbon nanotube (CNT) or Boron Nitride nanotube (BNT) filled with a linear chain of C_{60} called a "peapod"[35]. HRTEM images obtained using peapod or other methods confirmed the predicted theoretical spherical structure of C_{60} molecules as shown in Figure 1.4.

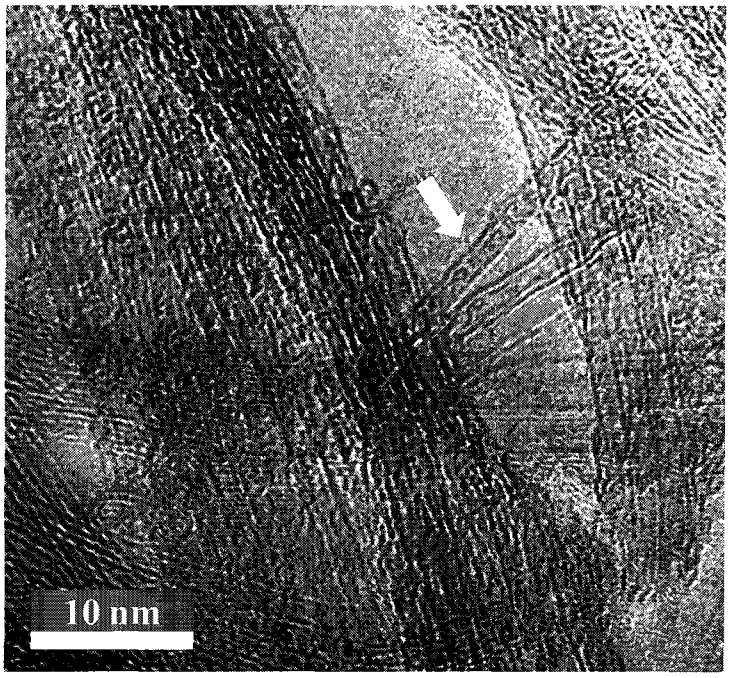

Figure 1.4 An HRTEM image of a single-walled carbon nanotube filled with a linear chain of C_{60} particles. Image by: Benjamin W. Jacob.

The core loss EELS spectra of C_{60} fullerenes showed two major sharp K-edges around 284 and 293 eV that correspond to a pure sp^2 carbon material[36,37]. It is noted that

special care must be taken during EELS investigation of C_{60} samples to ensure that the carbon lacey film support is not included in the spectrum.

The tribological performance of C_{60} molecules was also reported in the literature. Pure C_{60} films reveal relatively high friction coefficients (0.55 – 0.8) when tested under different loads and materials. It is believed that these high friction coefficients are due to the tendency of the C_{60} molecules to clump and compress into high shear strength layers rather than due to the impurities in the fullerenes. However, some experiments have shown lower friction coefficients for C_{60} particles when they are dissolved in some chemical solvents, such as benzene-solvated C_{60}. This improved frictional performance is believed to be due to the lowered shear strength of the hexagonal close-packed structure of the benzene-solvated C_{60} molecular crystals[38].

A typical Raman spectrum of C_{60} fullerenes is shown in Figure 1.5 (a-b)[39]. It is difficult to avoid the production of a C_{60}/C_{70} mixture during synthesis and therefore the sample was purified using a column chromatography. The absence of an intense C_{70} Raman band at 1569 cm^{-1} confirmed the absence of C_{70}, and the C_{60} sample purity. Among the eight clear C_{60} Raman bands, three strong ones were observed. The results revealed eight clear Raman bands and several weaker ones between 200 and 1600 cm^{-1}. The first strong Raman band was observed at 273 cm^{-1}, which corresponds to the predicted H_g squashing mode[30]. The two other strong Raman bands that appear at 496 and 1470 cm^{-1} correspond to totally symmetric breathing A_g modes[30].

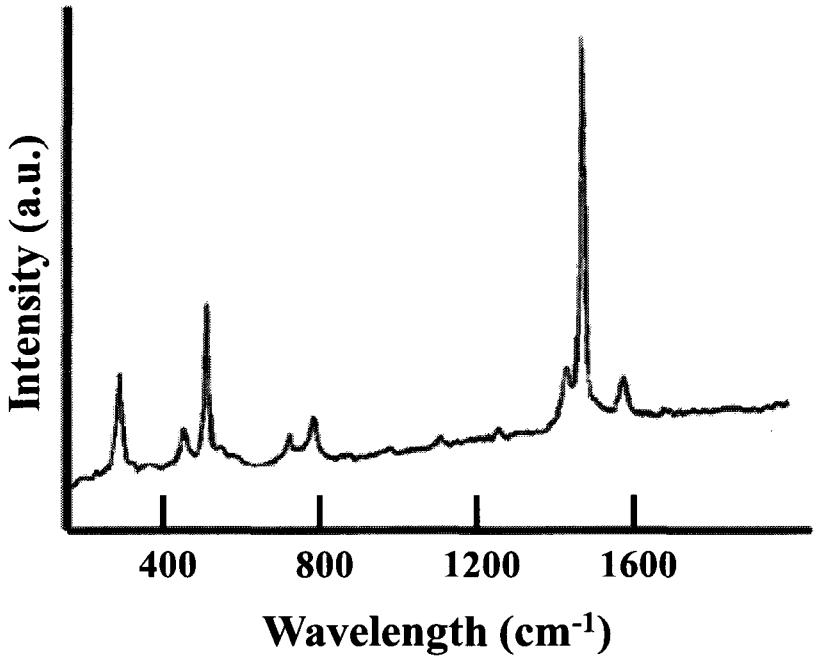

Figure 1.5 Raman spectra of a film of purified C_{60} [39].

1.1.3. Nanocrystalline Diamond (NCD)

In addition to C_{60} particles, nanocrystalline diamond (NCD), which was discovered in the early 1960s in the former Soviet Union[40], was used as the starting material for preparing the carbon onions. This nanomaterial, whose core is purely sp^3 bonded carbon[41], can be grown using different techniques, such as chemical vapor deposition (CVD)[42] and detonation of carbon-containing explosives[43]. The latter technique produces NCD as a power. In this research, the term NCD refers to the NCD powders produced using the detonation method. The powder is composed of particles having an average size of 5 nm as shown in Figure 1.6. Each particle consists of a diamond core that is partially or completely surrounded by layers of graphitic and/or amorphous carbon. This carbon nanomaterial, which can be produced in large commercial quantities, is also anticipated to combine an active surface (large surface to

volume ratio) having similar properties to those of macroscopic diamond, such as the diamond's hardness and Young's modulus, chemical stability, high thermal conductivity, and electrical resistivity[41].

NCD is used in composite materials like lubricants[44], and it has many potential medical, chemical, and electrical applications[42,45]. The performance of its applications is affected by the inability to provide particles having well-controlled surface chemistry.

The detonation synthesis method, used to produce NCD, results in raw soot containing NCD particles and other non-diamond carbons. To date, producing pure sp^3 NCD is a challenge due to the absence of an easy and cost effective purification treatment method[46].

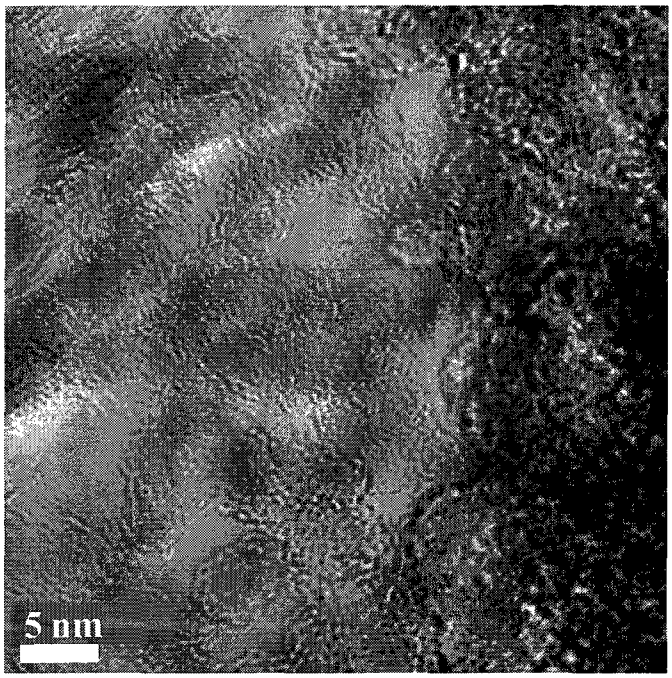

Figure 1.6 An HRTEM image of NCD particles having an average size of 5 nm. Image by: Raied A. Al-Duhileb.

The electronic properties and chemical structures of purified NCD particles has been reported in the literature[36]. EELS core loss spectra showed results that had a single peak at 289 eV, and were free of sp^2 bonded carbon as shown in Figure 1.7.

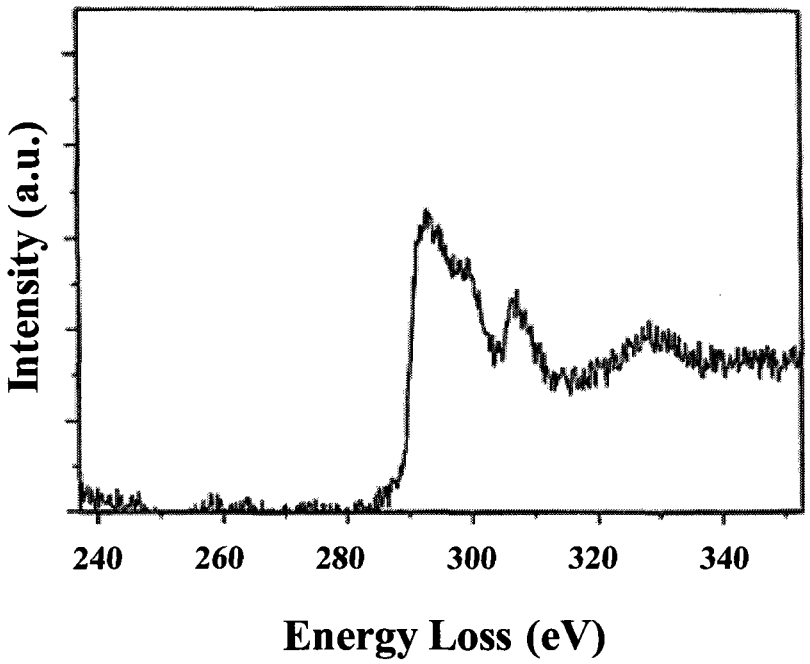

Figure 1.7 EELS core loss spectra of purified NCD particles. Results revealed a single peak at 289 eV and were free of sp^2 bonded carbon[41].

Purified NCD revealed vibrational Raman spectra as shown in Figure 1.8. The results showed four (4) clear Raman bands and several weaker ones at a range between 500 and 1650 cm^{-1}. The first strong Raman band, observed at 500 cm^{-1}, corresponds to amorphous sp^3 bonded carbon. The second peak, observed at 1090 cm^{-1}, corresponds to diamond surface phonons. The third peak, observed at 1325 cm^{-1}, corresponds to sp^3 carbon. The last strong peak, observed at 1620 cm^{-1}, was assigned to localized <1 0 0> sp^2 bonded pairs of carbon.

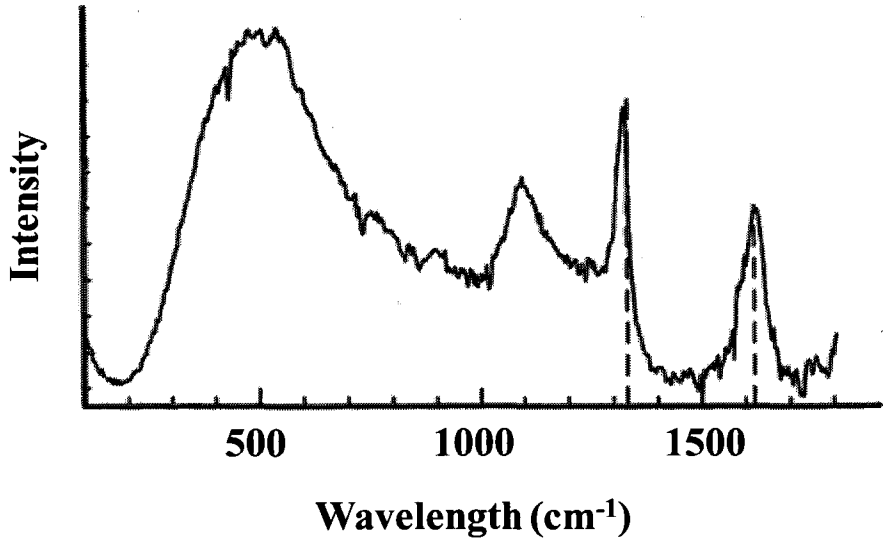

Figure 1.8 A Raman spectrum of NCD[41].

The tribological performance of the NCD films (~0.01-0.05)[42,45] has been widely reported in the literature, whereas NCD particles are less studied, and they showed higher friction coefficients (~0.8)[3].

References

1. J. Yang and K. Groh, "Materials issues in the space environment", Material Research Society Bulletin **34**: 12-16 (2010).

2. A. Hirata and N. Yoshioka, "Sliding friction properties of carbon nanotubes coatings deposited by microwave plasma chemical vapor deposition", Tribology International **37**: 893–898 (2004).

3. A. Hirata, M. Igarashi, and T. Kaito "Study on solid lubricant properties of carbon onions produced by heat treatment of diamond clusters or particles", Tribology International **37**: 899–905 (2004).

4. B. Yen, "Influence of water vapor and oxygen on the tribology of carbon materials with sp^2 valence configuration", Wear **192**: 208-215 (1996).

5. W, Zhao, J. Tang, A. Puri, R. Sweany, Y. Li, and L. Chen , "Tribological properties of fullerenes C_{60} and C_{70} microparticles", Journal of Materials Research **11**: 2749-2756.

6. D. Ugarte, "Curling and closure of graphitic networks under electron-beam irradiation", Nature **359:** 707-715 (1992).

7. D. Ugarte, "Formation mechanism of quasi-spherical carbon particles induced by electron bombardment", Chemical Physics Letters **207**: 473-481 (1993).

8. C. Mantell, Carbon and Graphite Handbook, (Interscience Publishers, New York, 1968).

9. H. Kroto, J. Heath, S. Obrien, R. Curl, and R. Smalley, "C_{60}: Buckminsterfullerene", Nature **318**: 162 (1985).

10. S. Mraz, "A new buckyball bounces into town", machinedesign.com, (2005).

11. S. Iijima, "Helical microtubules of graphitic carbon", Nature **354**: 56 (1991).

12. J. Viecelli, and F. Ree, "Carbon particle phase transformation kinetics in detonation waves", Journal of Applied Physics **88**: 683 (2000).

13. J. Viecelli, S. Bastea, J. Glosli, and F. Ree, "Phase transformations of nanometer size carbon particles in shocked hydrocarbons and explosives", The Journal of Chemical Physics **115**: 2730 (2001).

14. D. Tomanek and M. Schluter, "Growth regimes of carboncClusters", Physical Review Letters **67**: 2331 (1991).

15. M. Zwanger and F. Banhart, "The structure of concentric-shell carbon onions as determined by high-resolution electron microscopy", Philosophical Magazine B-Physics of Condensed Matter Statistical Mechanics Electronic Optical and Magnetic Properties **72**: 149-157 (1995).

16. A. Barnard, "Theory and modeling of nanocarbon phase stability", Diamond and Related Materials **15**: 285-291 (2006).

17. A. Barnard and P. Zapol, "A model for the phase stability of arbitrary nanoparticles as a function of size and shape", The Journal of Chemical Physics **121**: 4276 (2004).

18. V. Kuznetsov, A. Chuvilin, Y. Butenko, I. Mal'kov, and V. Titov, "Onion-like carbon from ultra-disperse diamond", Chemical Physics Letters **222**: 343-348 (1994).

19. N. Park, K. Lee, S. Han, J. Yu, and J. Ihm, "Energetics of large carbon clusters: crossover from fullerenes to nanotubes", Physical Review B **65**: 121405 (2002).

20. S. Tomita, T. Sakurai, H. Ohta, M. Fujii, and S. Hayashi, "Structure and electronic properties of carbon onions", The Journal of Chemical Physics **114**: 7477 (2001).

21. P. Schewe and B. Stein, "Carbon onions", Nature **22**: (1992).

22. S. Tomita, M. Fujii, S. Hayashi, and K. Yamamoto, "Electron energy-loss spectroscopy of carbon onions", Chemical Physics Letters **305**: 225-229 (1999).

23. H. Richter, T. Lada, V. Vejins, and J. Howard, "Large-scale production of fullerenes, carbon nanotubes and fullerenic Materials", Nano-C, Inc., 33 Southwest Park, Westwood, MA 02090, USA.

24. O. Mykhaylyka, Y. Solonin, D. Batchelder, and R. Brydson, "Transformation of nanodiamond into carbon onions: A comparative study by high-resolution transmission electron microscopy, electron energy-loss spectroscopy, x-ray diffraction, small-angle x-ray scattering, and ultraviolet Raman spectroscopy", Journal of Applied Physics **97**: 074302 (2005).

25. S. Osswald, G. Yushin, V. Mochalin, S. O. Kucheyev, and Y. Gogotsi, "Control of sp^3/sp^2 carbon ratio and surface chemistry of nanodiamond powders by selective oxidation in air", Journal of American Chemical Society, **128**: 11635-11642 (2006).

26. E. Obraztsova, M. Fujii, S. Hayashi, V. Kuznetsov, Y. Butenko, and A. Chuvilin, "Raman identification of onion-like carbon", Carbon **36**: 821-826 (1998).

27. M. Dresselhaus, G. Dresselhaus, R. Saito, and A. Jorio, "Raman spectroscopy of carbon nanotubes", Physics Reports **409**: 47-99 (2005).

28. H. Zhang, , G. Lin, Z. Zhou, X. Dong, and T. Chen, "Raman spectra of MWCNTs and MWCNT-based H_2-adsorbing system", Carbon **40**: 2429-2436 (2002).

29. P. Zhou, K. Wang, Y. Wang, P. Eklund, M. Dresselhaus, G. Dresselhaus, and R. Jishi, "Raman scattering in C_{60} and alkali-metal-saturated C_{60}", Physical Review B **46**: 2595–2605 (1992).

30. G. Adams, J. Page, O. Sankey, K. Sinha, J. Menendez, and D. Huffman, "First-principles quantum molecular-dynamics study of the vibrations of icosahedral C_{60}", Physical Review B **44**: 4052–4055 (1991).

31. K. Hedberg, L. Hedberg, D. Bethune, C. Brown, H. Dorn, R. Johnson, and M. Vries, "Bond lengths in free molecules of buckminsterfullerene, C_{60}, from gas-phase electron diffraction", Science **254**: 410 – 412 (1991).

32. B. Yadav and R. Kumar, "Structure, properties and applications of fullerenes", International Journal of Nanotechnology and Applications **2**: 15-24 (2008).

33. V. Bezmel'nitsyn, A. Eletskii, and M. Okun', "Fullerenes in solutions", Physics-Uspekhi **41**: 1091(1998).

34. www.sesres.com/PhysicalProperties.asp, March 2010.

35. A. Zettl, J. Cumings, Wei-qiang Han, and W. Mickelson, "Boron nitride nanotube peapods", The American Institute of Physics, 140-144 (2002).

36. P. Hansen, P.Fallon and W. Kritschmer, "An EELS study of fullerite - C_{60}/C_{70}", Chemical Physics Letters **181**: 367-372 (1991).

37. A. Papworth, C. Kiely, A. Burden, S. Silva, and G. Amaratunga, "Electron-energy-loss spectroscopy characterization of the sp^2 bonding fraction within carbon thin films", Physical Review B **62**: 12628–12631 (2000).

38. W. Zhao, J. Tang, A. Puri, R. Sweany, Y. Li, and L. Chen, "Tribological properties of fullerenes C_{60} and C_{70} microparticles", Material Research Society **11**: 2749-2756 (1996).

39. D. Bethune, G. Meijer, W. Tang, H. Rosen, W. Golden, H. Seki, C. Brown, and M. de Vries, "Vibrational Raman and infrared spectra of chromatographically separated C_{60} and C_{70} fullerene clusters", Chemical Physics Letters **179**: 181-186 (1991).

40. V. Danilenko, "On the history of the discovery of nanodiamond synthesis", Physics of the Solid State **46**: 595-599 (2004).

41. S. Prawer, K. Nugent, D. Jamieson, J. Orwa, L. Bursill, and J. Peng, "The Raman spectrum of nanocrystalline diamond", Chemical Physics Letters **332**: 93-97 (2000).

42. A. Sumant, O. Auciello, R. Carpick, S. Srinivasan, and J. Butler, "Ultrananocrystalline and nanocrystalline diamond thin films for MEMS/NEMS Applications". Material Research Society Bulletin **35**: 281-288 (2010).

43. V. Danilenko, Synthesizing and sintering of diamond by explosion, (Energoatomizdat: Moscow, 2003).

44. N. Red'kin, "Lubricants with ultradisperse diamond–graphite powder", Chemistry and Technology of Fuels and Oils **40**: 164-170 (2004).

45. D. Gruen, O. Shenderova, and A. Vul', Synthesis, properties and applications of ultrananocrystalline diamond, (Springer: Dordrecht, Netherland, 2005).

46. V. Dolmatov, "Detonation synthesis ultradispersed diamonds: properties and applications", Russian Chemical Reviews **70**: 607-626 (2001).

Chapter 2

Characterization Instruments and Methods

Many instruments and methods are currently being used to investigate the fundamental properties of novel nano-materials. These instruments and methods have recently been developed in response to the expanding need to further explore and characterize these newly discovered materials at the nanoscale. In this research, several material characterization instruments were used to analyze the structural, chemical and electronic properties of carbon onions, C_{60}, and NCD. This chapter explains the fundamental principles of the instruments utilized to characterize the nano-materials in this research.

2.1. Transmission Electron Microscopy[1,2]

Transmission Electron Microscopy (TEM) is an important technique that is widely used for nanoscale characterization. It can achieve very high spatial resolution (~0.2 nm), and is used for obtaining highly magnified images, material chemical compositions, and electronic structures.

In this technique, a beam of highly accelerated electrons is focused on a very thin (< 100 nm) specimen. The deflected and undeflected electrons that penetrate the sample are collected to generate the TEM signal. Because electrons tend to bend in the TEM column, a series of magnetic lenses are positioned above and below the sample to bring a

parallel electron beam to a focal point. The generated TEM signal can be magnified as little as 50 times to as much as a million times. This superior magnification is achieved due to the small wavelength of electrons (~0.0037 nm) that result in better resolution capabilities. The wave nature of an electron (λ) is given by de Broglie's relation:

$$\lambda = \frac{h}{p} = \frac{h}{\sqrt{2m_0qV}} \cdot \frac{1}{\sqrt{1+\frac{2qV}{m_0c^2}}}, \tag{2.1}$$

where h is Plank's constant 6.6 x 10^{-34} J.s, p is the electron momentum, m_0 is the electron rest mass 9.1 x 10^{-31} kg, q is the fundamental electron charge 1.6 x 10^{-19} C, and V is the TEM operating acceleration voltage. The relationship, given in Equation 2.1, includes the relativistic correction required by the high velocities that the electrons achieve during acceleration in the TEM column.

The TEM system anatomy is illustrated in Figure 2.1, showing the location of the thin sample, electromagnetic lenses, the electron gun and the imaging and recording system within the TEM. The diffraction-limited spatial resolution of two individual points in the TEM system is given by Abbe's Equation:

$$\text{Resolution Power} = \frac{0.61\,\lambda}{n \sin \alpha}, \tag{2.2}$$

where λ is the wavelength of the electron, n is the refractive index and α is the acceptance angle. The 0.61 factor describes Resolution Power in a TEM system, and it includes the

theoretical diffraction limit and the additional limits introduced by the objective and condenser lenses. The small wavelength of electrons results in a smaller and better resolution capability. This simply suggests that TEM instruments operating at higher accelerating voltages or energies provide a significant reduction in the minimum resolvable spacing since the electron wavelength is inversely proportional to the momentum, which is directly proportional to the amount of energy.

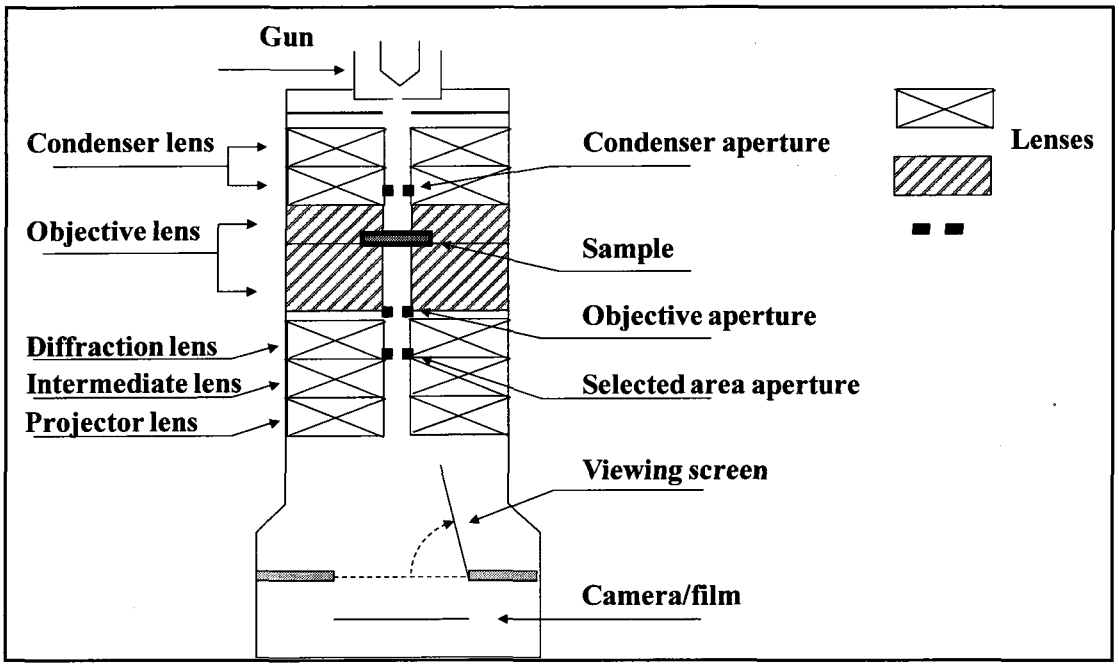

Figure 2.1 The TEM anatomy. The thermionic or field emission electron gun emits a beam of focused electrons that penetrate the thin sample. The magnetic condenser, objective, diffraction, intermediate, and projector lenses control the electron beam and bring it to a focal point. Electrons that pass the sample are collected and the image is shown on the viewing screen or camera.

TEM instruments that operate on high accelerating voltages have improved penetration ability because highly energetic electrons interact less with matter than low-energy electrons. Therefore, analyzing thicker samples is achievable using high-voltage TEM instruments. The quality of electron penetration is obtained by measuring the mean

distance between scattering events. The fewer elastic and inelastic scatterings yield a farther electron penetration into the sample.

Despite its great advantages, TEM has limited depth resolution, causing images to be projected onto a two-dimensional detector. The structural information along the beam direction of multi-structural features is superimposed at the image plane, which results in a convolution of the scattering contrast. The image contrast from a sample region must be deconvolved in order to determine overlapping microstructural features of a given object. It addition, TEM does not have an inherent ability to differentiate between atomic species. In order to overcome this drawback, TEM instruments are often equipped with other tools and techniques that distinguish between different atomic species by measuring the deflection angles of scattered electrons.

2.1.1. TEM Operation[1,2]

TEM instruments have two methods to view the sample: image mode and diffraction mode.

In the image mode, the scattered electrons are utilized to create the image details and atomic structure. Conventional TEM instruments have three different image modes: bright-field microscopy, dark-field microscopy, and high resolution transmission electron microscopy (HRTEM). In the bright-field mode, the diffracted electrons are blocked using a small objective aperture, which only passes the un-diffracted (forward) electrons. This mode provides higher intensity, lower contrast, and better focusing. In the dark-field mode, in contrast, the diffracted electrons are allowed to pass beside the forward electrons through the objective aperture. The dark-field image is not always a direct

reversal of the bright-field mode, and sometimes reveals more structural details. In the HRTEM mode, a larger objective aperture is used to pass all electrons, which recombine in the image forming process to create high resolution images. This mode enables the user to thoroughly investigate the local structural details of different materials.

In the diffraction mode, a diffraction pattern is formed on the back focal plane of the objective lens. The diffracting volume (i.e. diffracted electrons) is limited by using a selected-area aperture, which results in many spots or reflections as shown in Figure 2.2. This technique is called selected-area diffraction (SAD) or selected-area electron diffraction (SAED).

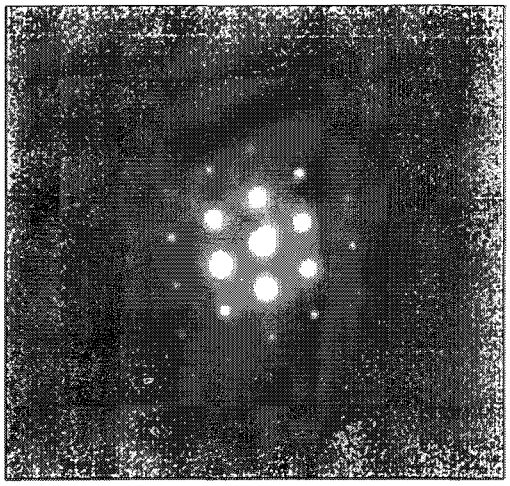

Figure 2.2 Typical diffraction pattern (single crystal pattern).

By measuring the relative distances and angles of the diffraction spots the crystal structure of a particular area of the sample can be determined. The atomic lattice spacing (d) is given by the relation:

$$d = \frac{\lambda.L}{R}, \tag{2.3}$$

where λ is the electron wavelength, L is the camera length, and R is the relative distance between the diffraction spots as shown in Figure 2.3. The results of the diffraction mode analysis reveal one of the three typical diffraction patterns: single crystal, poly-crystal, or amorphous.

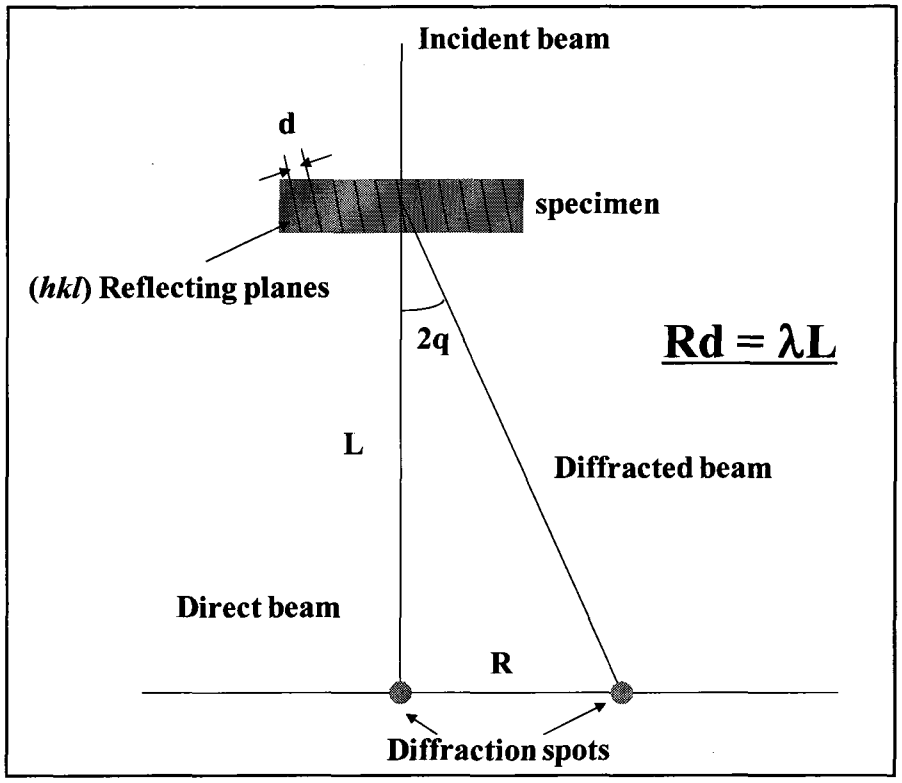

Figure 2.3 Determining the atomic lattice spacing (d) in diffraction mode using wave length of the electron (λ), camera length (L), and relative distance between the diffraction spots (R).

In this research, high resolution images of the internal structures of carbon onions, C_{60}, and NCD were obtained using a JEOL 2200FS field emission TEM operated at 200 kV at the Center for Advanced Microscopy at Michigan State University.

2.2. Scanning Electron Microscopy[1,2]

The scanning electron microscope (SEM) is another important tool for investigating the structural properties of materials. It has an improved resolution that can approach a few nm, and high magnification capabilities that can reach up to 300,000x. It obtains images of different samples using an electron beam that can be accelerated at 15 kV. Although SEM has some operational features that are similar to TEM, the SEM electron beam can interact with the sample surface (~ 5 nm), whereas electrons penetrate and pass through the sample in TEM. Therefore, the SEM can investigate the surfaces of samples that are thicker (> 100 nm) than those required by the TEM (< 100 nm).

The SEM electron beam, which is produced in a vacuum using either a thermionic or a field emission electron gun, is focused on a particular area of the sample surface. The SEM produces three types of images, namely secondary electron images, backscattered electron images, and X-ray mapping. These different images are due to the complex interactions that take place when an incident-beam electrons strike the surface of a sample.

In secondary electron imaging, the incident-beam electrons transfer part of their energy to the electrons of the sample. This creates low energy (average energy of about 3 eV) secondary electrons that are capable of escaping the sample surface. The emitted secondary electrons are partially collected using an electron detector at an angle to the

sample, and used to produce mapped images on a cathode ray tube (CRT) as shown in Figure 2.4[3].

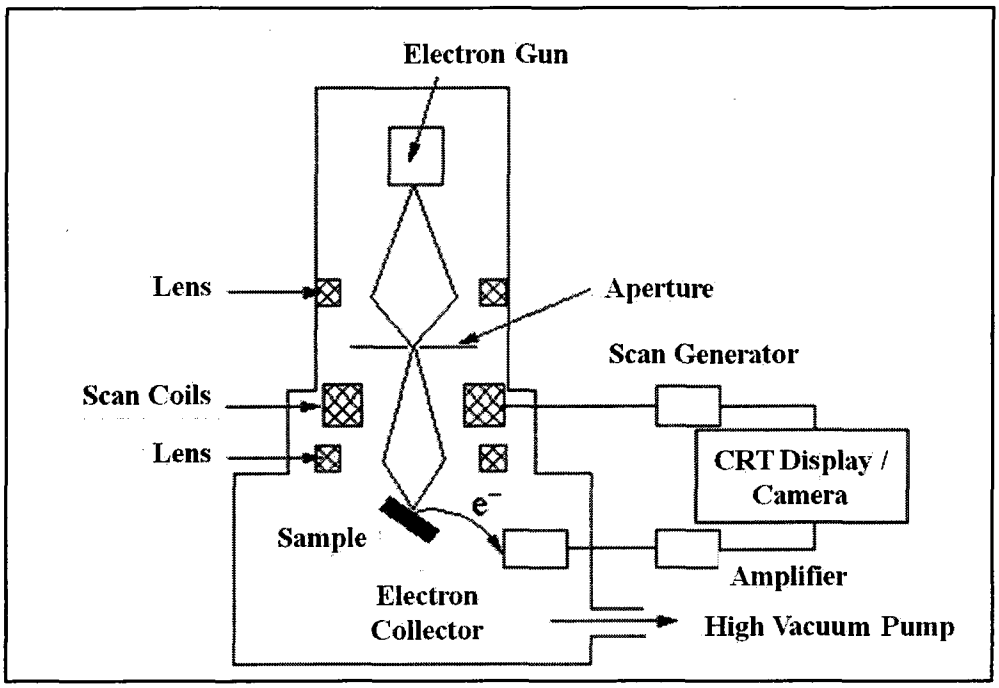

Figure 2.4 A schematic diagram illustrating the basic components and operation of an SEM. An electron gun focuses an electron beam on the surface of the sample. This results in producing secondary electrons that are collected by special electron detector and displayed as a mapped image on a screen[3].

In the second imaging mode, backscattered electron imaging, a considerable fraction of the beam electrons undergoes elastic interactions with the electrons of the sample. These interactions produce higher energy backscattered electrons (average energy of about 50 eV). Backscattered electrons are produced from the whole beam-sample interaction area, and therefore electrons from greater depths have sufficient energy to escape the sample. The maximum escape depth of the backscattered electrons is inversely proportional to the average atomic number (Z) of the sample. More backscattered electrons can escape samples having small atomic numbers, whereas fewer

backscattered electrons escape samples having large atomic numbers. Due to their large escape width (~ fraction of a micrometer), backscattered electrons result in a resolution lower than that produced using secondary electrons. A scintillator or semiconductor detector is positioned above the sample, and utilized to detect the high energy backscattered electrons.

The third imaging mode is energy dispersive X-ray spectroscopy (EDS). In addition to backscattered and secondary electrons, an inelastic interaction between the beam electrons and the sample electrons excites primary sample electrons at lower ground state atomic energy levels to higher energy shells in the atoms of the sample. When the excited electrons decay to their ground states, they emit X-ray photons, which have different energies and wavelengths ("energy dispersive"), from the entire beam-sample interaction area. Because each element in the periodic table requires a unique energy to excite the primary electrons to higher energy shells, the emitted X-ray signal is utilized to create elemental maps of the sample showing the spatial distribution of particular elements in the field of view. The X-ray photons are detected by a photon detector that is attached to the column of the SEM.

In this research, the sample uniformity of carbon onion, C_{60}, and NCD samples was investigated using Hitachi S-4700II field emission SEM (FESEM), which is equipped with an EDAX Phoenix energy dispersive X-ray spectrometer system for microanalysis, a chamber scope for direct chamber viewing and a backscattered electron detector for Z contrast, at the W. M. Keck Microfabrication Facility (KMF) at Michigan State University.

2.3. Electron Energy Loss Spectroscopy[1,2,4]

Electron energy loss spectroscopy (EELS) is a method for analyzing the energy distribution of elastic and inelastic scattered electrons that pass through a thin sample characterized by TEM or scanning transmission electron microscope (STEM). This useful technique provides elemental quantifications and electronic structures of different samples. Compared to other material analytical techniques such as energy dispersive spectroscopy (EDS), EELS has very high sensitivity to light elements and spatial energy resolution of about 1 eV.

The spectral profile or signature of EELS is characterized by the amount of energy that an electron loses when passing through a thin specimen. Electrons within the sample atoms accept specific values of energy and are promoted to higher empty state levels (conduction bands). This causes electrons of the TEM accelerated beam to lose part of their energy. The lost energy is equivalent to the energy transferred to the sample electrons as shown in Figure 2.5.

To obtain EELS spectra, inelastic scattered electrons that interact with the inner shell electrons of the sample and lose part of their energy, and elastic scattered electrons that interact with the atomic nuclei and do not lose energy are analyzed using a magnetic prism as shown in Figure 2.6.

In this process, the scattered electrons pass through a uniform magnetic field generated by the magnetic prism. Inelastic scattered electrons exhibit smaller bending radii, whereas elastic scattered electrons reveal lager bending radii corresponding to their higher energy and velocity. The bending radius of an accelerated electron is given by Equation (2.4):

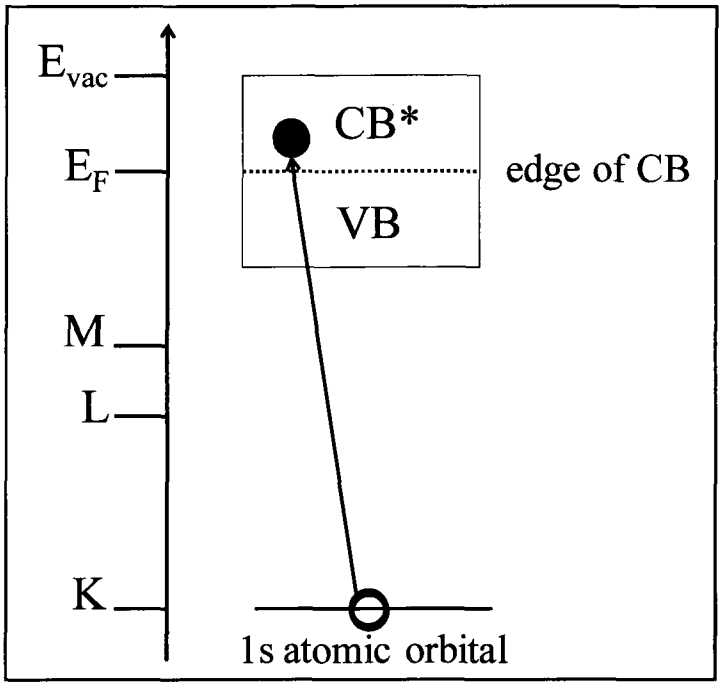

Figure 2.5 Energy level diagram showing excitation from the inner shell (valance band) into the empty state higher shell (conduction band)[1].

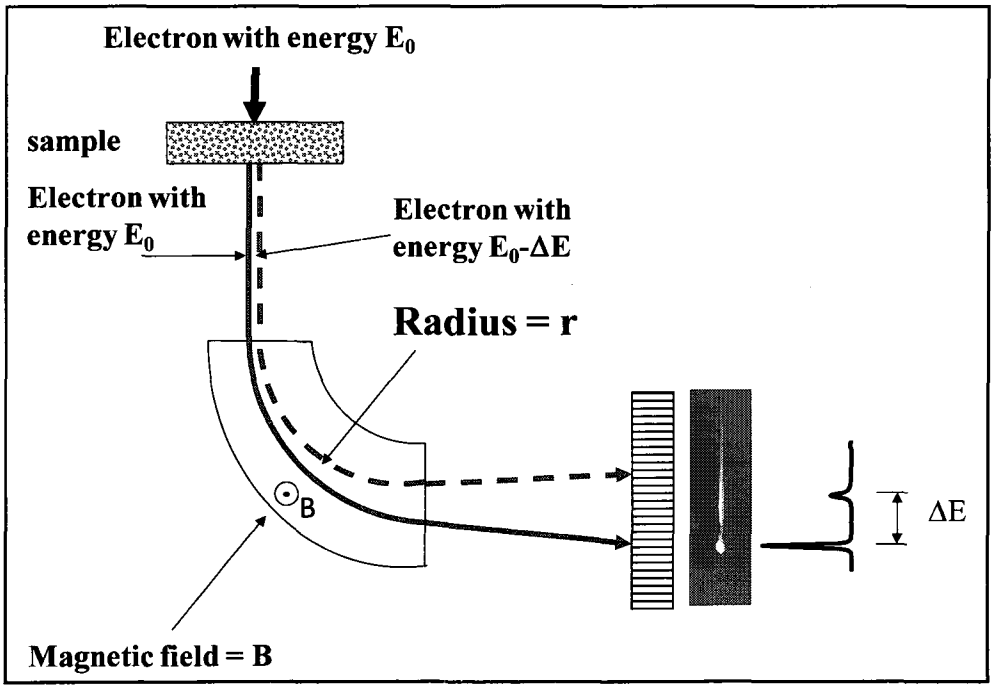

Figure 2.6 The magnetic prism is used to record the intensity of scattered electrons at different position to obtain the energy loss spectrum.

$$\text{radius (r)} = \frac{\gamma \cdot m_0 \cdot v}{q \cdot B}, \qquad (2.4)$$

where m_0 is the rest mass of an electron, v is the velocity of an accelerated electron, q is the unit electronic charge 1.6 X 10^{-19} C, and B is the magnetic field . The intensity of the scattered electrons is recorded at different positions, which are then used to obtain the EELS spectra.

Each element in the periodic table has a unique inner-shell ionization edge that corresponds to the energy required for prompting an inner-shell electron to empty states above the Fermi level as shown in Figure 2.7. On the experimental spectra, the edge energy is determined at the point where the first derivative is the maximum or the second derivative is zero.

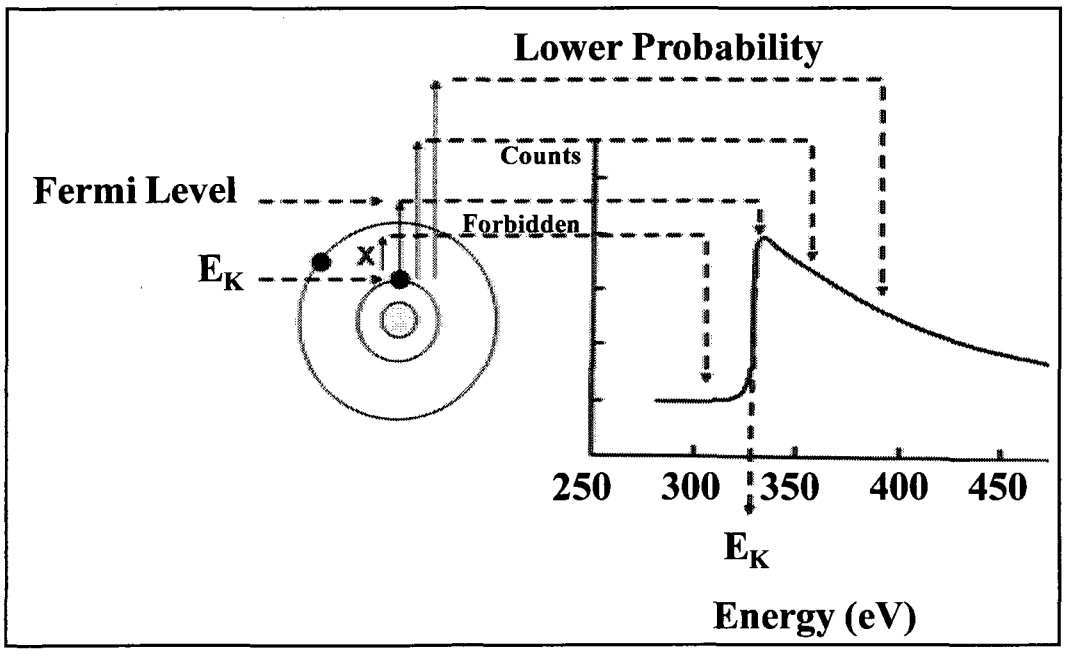

Figure 2.7 A schematic diagram illustrating the shape of the inner-shell ionization edge of an element in the periodic table.

The theory of elemental quantification is used in EELS to determine the precise chemical compositions of a sample based on the differences between the inner-shell binding energies of chemical elements. To quantify an inner-edge (K, L or M) in a given sample, it is assumed that the inner-shell single scattering intensity (I_{inner}) is related to the total intensity (I_T) by Equation 2.5:

$$I_{inner} = P_{inner} I_T, \tag{2.5}$$

where P_{inner} is the probability of transition, and given by Equation 2.6:

$$P_{inner} = N \sigma_{inner} I_T, \tag{2.6}$$

where σ_{inner} is the inner-shell ionization cross-section and N is the areal density of atoms (atoms / unit area).

These mathematical relationships can be extended to a spectrum with multiple edges corresponding to different chemical compositions. For example, the expression for analyzing the k-ionization edges of a sample having two elements A and B is given by Equation 2.7:

$$\frac{N_A}{N_B} = \frac{I_K^A \cdot \sigma_K^B}{I_K^B \cdot \sigma_K^A}. \qquad (2.7)$$

This expression is also applicable for L- and M-ionization edges, and combinations of edges. Therefore, to measure the ratio of two elements or allotropes that are present in a sample, the areal intensities under EELS spectra of each element or allotrope should be obtained using special de-convolution (fitting) techniques, and analyzed using Equation 2.7.

Users may experience some difficulties in obtaining EELS spectra if the sample is too thick and/or the TEM beam is unstable. Care should be taken in preparing samples for EELS analysis, and the beam should be in the standby mode for at least eight hours to maximize its stability.

The powerful EELS capability is employed in this research to analyze the bond hybridization (i.e., the sp^2/sp^3 ratio) of the carbon onion samples as a function of synthesis temperature. Because EELS can achieve very high spatial resolution, and is highly sensitive to the different bond structures within a sample, it can accurately quantify of the nature of the bonding present in the carbon systems.

In this research, EELS experiments were performed using an integrated Omega filter in a JEOL 2200FS. The energy resolution was around 1.5 eV, evaluated using the full width half max (FWHM) of the zero loss peak. EELS spectra were first corrected for instrument background and plural scattering using Gatan analysis software. The corrected spectra were then analyzed using a deconvolution technique based on asymmetric f-variance area (Peak Fit™ by SigmaPlot, version 4.12). The use of the asymmetric f-

variance area to describe the K-edge versus a symmetric Gaussian description is an original contribution of this thesis[5].

2.4. Raman Spectroscopy[1,6]

The bonding nature of solid samples can also be studied using Raman spectroscopy. This technique sets the atoms of a solid sample into vibration modes (phonons), which depend on the atomic masses and bond force constants of the sample atoms, using a laser beam (photons). The laser beam photons are often elastically scattered when they interact with electrons of the sample. This elastic interaction between the laser beam and the sample's electrons is called Rayleigh scattering. Less frequently, the photons of the laser beam scatter inelastically and lose part of their initial energy when interacting with the sample's electrons. This inelastic interaction between the photons of the laser beam and the electrons of the sample takes place by one of two methods, namely Stokes scattering and anti-Stokes scattering. In Stokes scattering, the sample's electrons are promoted to higher energy states because the incident laser beam photons transfer part of their energy to them. As a result, the scattered laser beam photons will have less energy and a longer wavelength than the incident beam laser photons, as shown in Figure 2.8. The difference in wavelengths of the incident and scattered laser beam photons, which is called Raman shift, is used to determine the elemental composition of the sample because each element in the periodic table exhibits a unique spectrum and Raman shift.

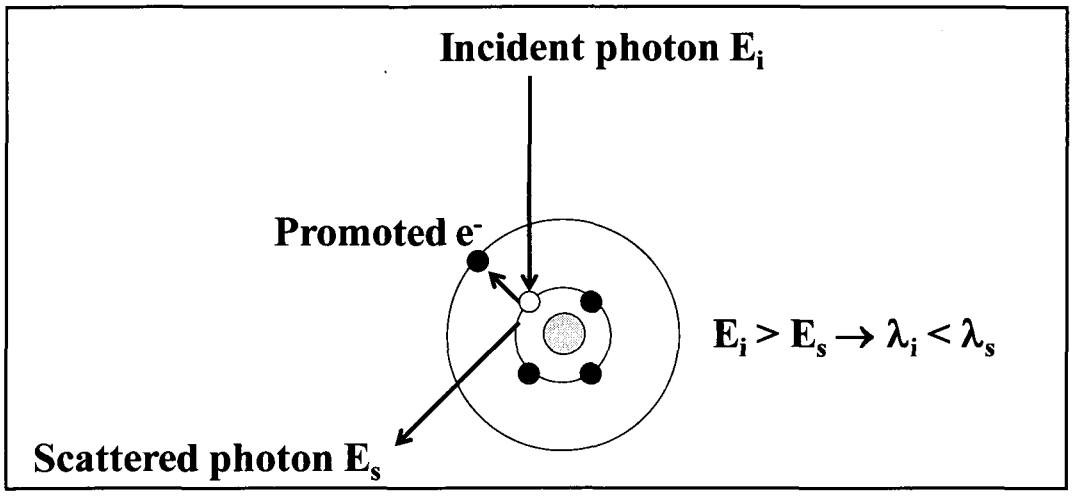

Figure 2.8 Excitation of an inner-shell electron by incident light beam photons. The energy of the scattered light beam photons is less than the energy of the incident laser beam photons.

In anti-Stokes scattering, scattered laser beam photons gain some energy when the excited electrons of the sample, which are at higher energy states, drop down to lower vibration energy states and release part of their energy. This causes the wavelength of the scattered laser beam photons to be shorter, and their energy to be higher. This process is a mirror of the Stokes scattering on the opposite side of the Rayleigh line as shown in Figure 2.9[7]. Because this process strongly depends on temperature, anti-Stokes scattering is usually not measured, and does not contribute to a Stokes Raman spectrum.

Each element exhibits a unique Raman spectrum, which corresponds to a distinctive phonon mode, when the sample interacts with laser beam photons. Therefore, Raman spectroscopy is used in this research to further analyze the different allotropes of carbon: carbon onions, C_{60}, and NCD. Room temperature Raman spectroscopy experiments were performed using the Kaiser Optical micro Raman Spectrograph that uses a frequency-doubled yttrium aluminum garnet (YAG) laser with a wavelength of

532 nm, and is available at the W. M. Keck Microfabrication Facility (KMF) at Michigan State University.

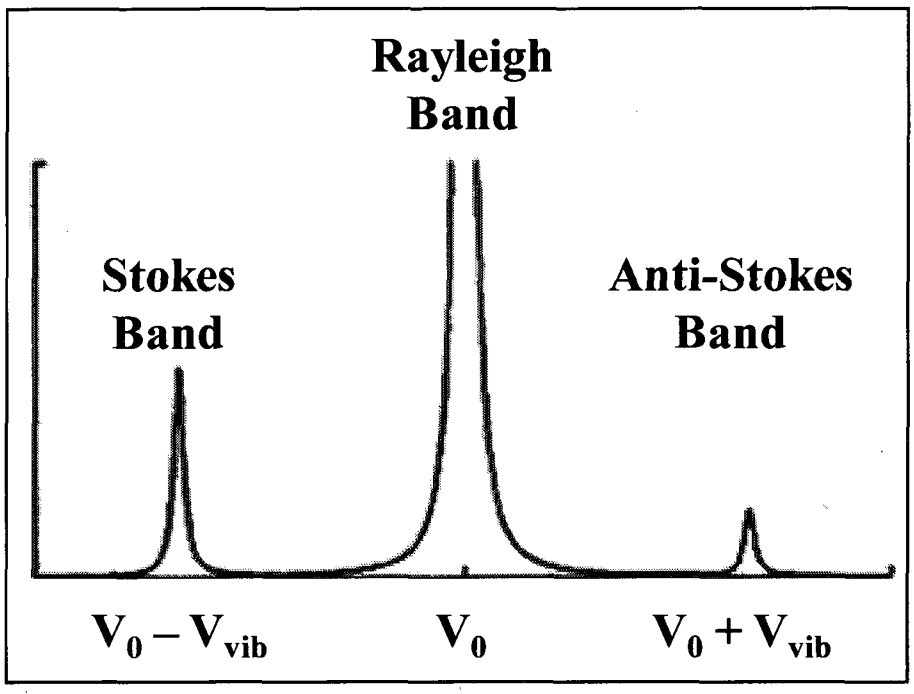

Figure 2.9 A schematic Raman scattering spectrum showing Rayleigh line, Stokes scattering, and anti-Stokes scattering[7].

2.5. Sample Preparation Methods

The accuracy of the material characterization instruments strongly depends on the preparation quality of the analyzed specimens. The preparation procedures are crucial and require special care to obtain high-quality results. This section outlines the different sample preparation methods that were followed to perform the experimental part of the research.

2.5.1. TEM, SEM, and EELS Samples

Carbon onions were prepared from crystalline diamond nanoparticles having an average diameter of 5 nm. The diamond nanoparticles were heated in inert ambience in an infrared gold image furnace. A graphite holder filled with 10 mg of diamond nanoparticles was placed inside a furnace evacuated to approximately 1.3 Pa with a rotary pump, and slowly heated in argon gas flow at 1.5×10^5 Pa to 1700°C, 2000°C and 2300°C, respectively. The furnace temperature was held for 60 s and then gradually cooled to room temperature in argon flow. The C_{60} and NCD (Cheap Tubes Inc., Brattleboro, VT) samples were acquired commercially, and were 99wt% pure.

To prepare the samples for TEM, SEM, and EELS analysis, these carbon nano-materials were suspended in ethyl alcohol, sonicated, and then dispersed onto carbon lacey film 200 mesh copper grids (SPI Supplies, West Chester, PA). Special care was taken to acquire an EELS spectrum of only the carbon onions and not the carbon lacey film. Large holes in the lacey film were utilized to ensure the EELS spectra contained only carbon onions.

References

1. C. Brundle, C. Evans, and S. Wilson, Encyclopedia of Materials Characterization, (Butterworth-Heinemann, Stoneham, MA, 1992).

2. S. Flegler, J. Heckman, and K. Klomparens, Scanning and Transmission Electron Microscopy: An Introduction, (Oxford University Press, New York, NY, 1993).

3. http://www.chm.bris.ac.uk/pt/diamond/stuthesis/chapter2.htm, January 2010.

4. R. Egerton, Electron Energy Loss Spectroscopy in the Electron Microscope, (Plenum Press, New York, NY, 1986).

5. R. Alduhaileb, V. Ayres, B. Jacobs, X. Fan, K. McElroy, A. Hirata, M. Horikoshi, N. Lehnert, and M. Galinato, "Carbon onion films-molecular interactions of multi-layer fullerenes", Materials Research Society Fall Meeting, Boston, MA, 2009.

6. R. McCreery, Raman Spectroscopy for Chemical Analysis, (A Wiley-Interscience Publication, New York, NY, 2000).

7. M. Denk, "Vibrational spectroscopy", CHEM 2070 - Structure and Spectroscopy, Guelph, Ontario N1G 2W1, Canada (2005).

Chapter 3

Carbon Atom Hybridization

The element carbon exists in several forms or allotropes in nature, and may form an enormous number of chemical compounds. This diversity is mainly due to the unusual number of bond types that this element can form with other carbon atoms and elements in the periodic table. Understanding the different bond types in carbon is essential for investigating the structural and frictional properties of carbon nano-materials, such as carbon onions, C_{60}, and NCD. Single-shell fullerene C_{60} and multi-shell fullerene carbon onions are almost purely sp^2 bonded carbon materials. On the other hand, the starting NCD particles used to prepare the carbon onion samples are almost purely sp^3 bonded carbon material. The original work in this research quantifies the ratio of the different hybridized bonding present in the carbon onions, and investigates the effect of bond hybridization on their tribological performance. This chapter introduces the basic chemical principles and bond hybridization types existing in nano-materials used in this research.

3.1. Hybrid Orbital Introduction[1,2,3,4]

The concept of orbital hybridization was introduced to explain the atomic orbital structures of some chemical compounds and molecules that exhibited unpredicted chemical shapes[4]. For instance, the early predicted shapes of the water molecule (H_2O),

ammonia (NH_3), and methane (CH_4), based on strict s- and p- orbital filling, did not coincide with the experimental outcomes.

The element carbon, the sixth element in the periodic table, has six electrons around the nucleus in an electron configuration ($1s^2\ 2s^2\ 2p^2$). The two core electrons in the innermost orbital (1s) are strongly tied to the nucleus, and require high energy to promote them to higher energy levels. The original assumption was that the two electrons in the 2s orbital were similarly in a closed shell and therefore inert. Carbon was expected to form bonds with two hydrogen (H) atoms using its remaining two electrons in two orthogonal 2p orbitals, resulting in two C-H bonds with a bond angle of 90° between them. However, the practical chemical experiments revealed several other hydrocarbon compounds including methane CH_4 with its four-fold tetrahedral C-H configuration. This phenomenon also took place in other chemical compounds such as BF_3 and BCl_3. To explain these unexpected results, chemists suggested that the 2s electrons must contribute in the formation of bonds between carbon and boron atoms, and other elements.

In reality, the small energy difference between the upper 2p and the lower 2s energy levels results in an opportunity to change the valence electron configuration of carbon from strict $[2s^2]\ 2p^2$ to a series of s-p orbital combinations by mixing the electronic wave functions of the 2s and 2p electrons (hybridization). The possible bond hybridizations for carbon are: sp, sp^2 and sp^3.

3.2. sp Hybrid Orbitals[1,2,3]

In the sp bond hybridization model, the 2s orbital is hybridized or mixed with one of the 2p orbitals ($2p_X$, $2p_Y$, or $2p_Z$). This mixture results in two of the valence electrons

being located in hybridized sp orbitals with two of the valence electrons located in unchanged p orbitals, as shown in Figure 3.1. The mixture of the 2s and 2p atomic orbital wave functions $|2s\rangle$ and $|2p\rangle$ can be mathematically represented by a linear combination as shown in Equations 3.1 and 3.2:

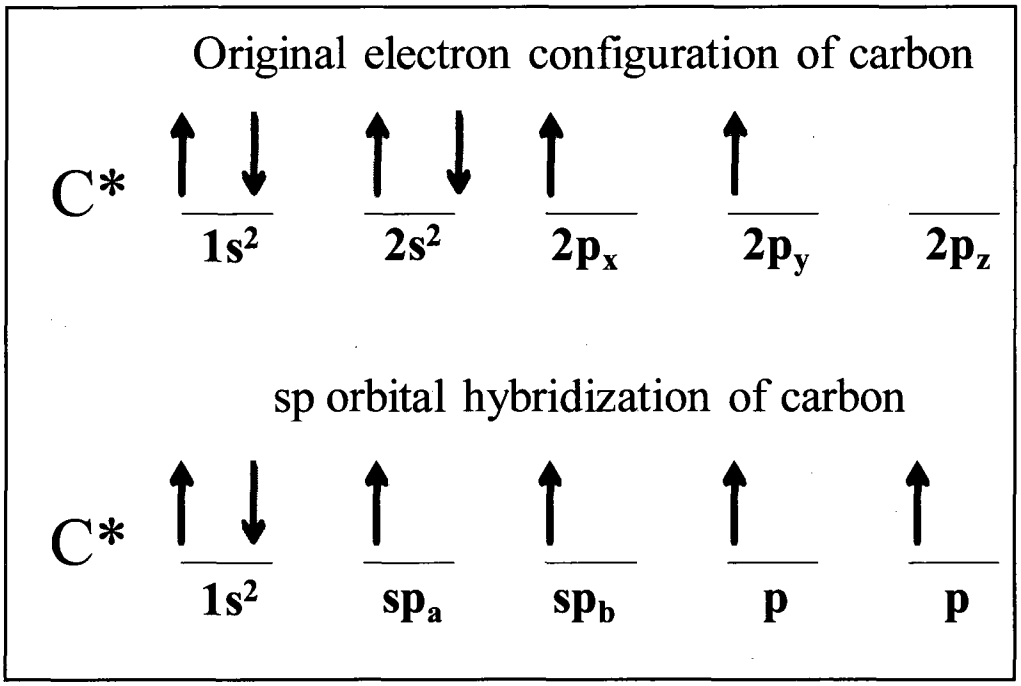

Figure 3.1 A hybridization model of sp orbitals. An electron is promoted to a higher empty state due to the small energy differences between the lower 2s and the upper 2p energy levels.

$$|sp_a\rangle = C_1 |2s\rangle + C_2 |2p_x\rangle \tag{3.1}$$

$$|sp_b\rangle = C_3 |2s\rangle + C_4 |2p_x\rangle, \tag{3.2}$$

where C_1, C_2, C_3, and C_4 are the mixing or linear combination coefficients[2]. These coefficients can be calculated using the orthonormality conditions: $\langle sp_a|sp_b\rangle = 0$,

$\langle sp_a|sp_a\rangle = 1, \langle sp_b|sp_b\rangle = 1$, and $(\langle sp_a|sp_a\rangle + \langle sp_b|sp_b\rangle)_{2s\ component} = 1$.

Solving for the unknown coefficients using these conditions yields the following results:

$C_1 = C_2 = C_3 = \frac{1}{\sqrt{2}}$, and $C_4 = -\frac{1}{\sqrt{2}}$. Equations 3.1 and 3.2 can therefore be rewritten as:

$$|sp_a\rangle = \frac{1}{\sqrt{2}} [|2s\rangle + |2p_x\rangle] \quad (3.3)$$

$$|sp_b\rangle = \frac{1}{\sqrt{2}} [|2s\rangle - |2p_x\rangle]. \quad (3.4)$$

The atomic orbitals of the new energy states (i.e., sp_a and sp_b) are centered on the atom, separated by 180°, and located in opposite directions as shown in Figure 3.2. These two orbitals have high electron probability, and two electrons of the same energy.

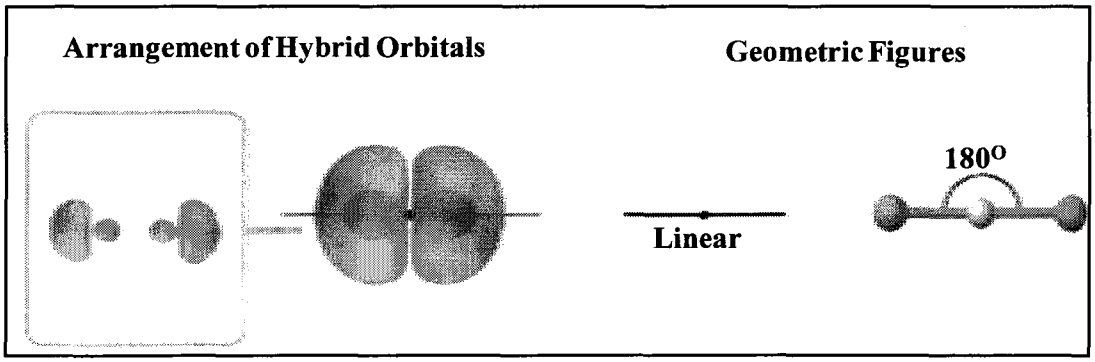

Figure 3.2 New atomic orbitals (i.e. sp_a and sp_b) resulting from mixing the 2s orbital with one of the 2p orbitals ($2p_x$, $2p_y$, or $2p_z$). The resulting energy states are located in opposite directions, and centered on the atom. Source: www.chem.umass.edu[5].

The triple bond between the two carbon atoms consists of one sigma (σ) bond, which is formed by the covalent overlap of sp hybrid orbitals, and two pi (π) bonds,

which are also covalent bonds but weaker than σ bonds because of the lesser degree of overlap[1]. The two π bonds are formed by the overlap of parallel $2p_y$ and $2p_z$ orbitals.

3.3. sp^2 Hybrid Orbitals[1,2,3]

In the sp^2 orbital hybridization model the 2s orbital is hybridized or mixed with two of the 2p orbitals ($2p_x$, $2p_y$, or $2p_z$). This results in three sp^2 orbitals and one unchanged p orbital as shown in Figure 3.3. The linear combination of the 2s and 2p atomic orbitals can be mathematically represented by Equations 3.5, 3.6, and 3.7:

$$|sp_a^2\rangle = C_1|2s\rangle - \sqrt{1-C_1^2}|2p_y\rangle \tag{3.5}$$

$$|sp_b^2\rangle = C_2|2s\rangle + \sqrt{1-C_2^2}\left[\frac{\sqrt{3}}{2}|2p_x\rangle + \frac{1}{2}|2p_y\rangle\right] \tag{3.6}$$

$$|sp_c^2\rangle = C_3|2s\rangle + \sqrt{1-C_3^2}\left[-\frac{\sqrt{3}}{2}|2p_x\rangle + \frac{1}{2}|2p_y\rangle\right], \tag{3.7}$$

where C_1, C_2, and C_3 are the mixture or linear combination coefficients. These coefficients are determined using the same orthonormal requirements applied to the (sp_i^2) and (2s components), which are given Equations 3.8, 3.9, and 3.10.

$$C_1^2 + C_2^2 + C_3^2 = 1 \tag{3.8}$$

$$C_1C_2 - \frac{1}{2}\sqrt{1-C_1^2}\sqrt{1-C_2^2} = 0 \tag{3.9}$$

$$C_1C_3 + \frac{1}{2}\sqrt{1 - C_1^2}\sqrt{1 - C_3^2} = 0. \quad (3.10)$$

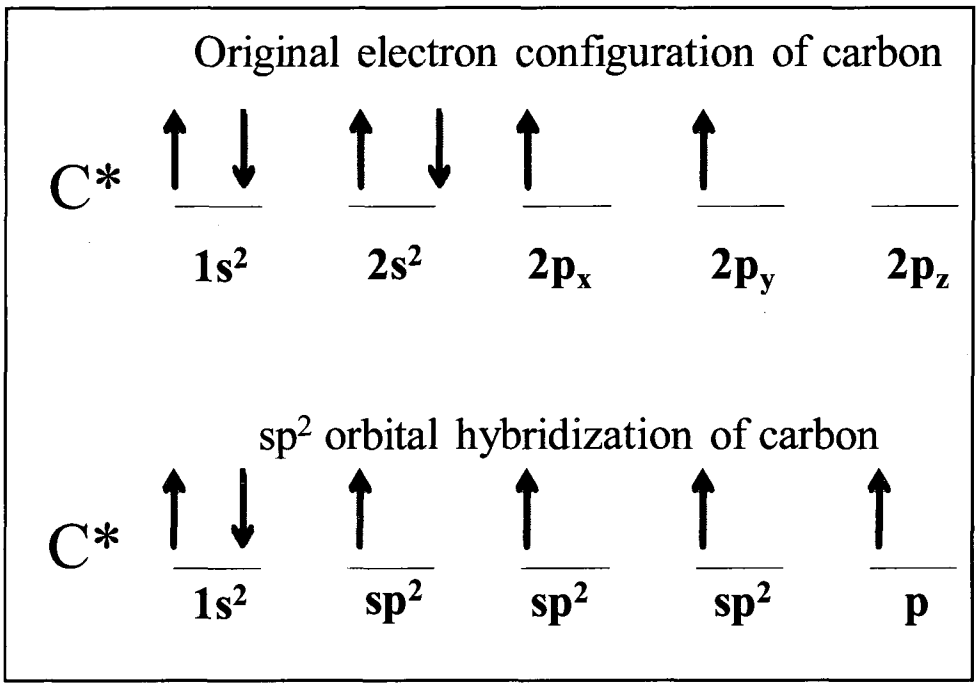

Figure 3.3 A hybridization model of sp^2 orbitals.

Solving for the unknown coefficients using these conditions yields the following results: $C_1 = C_2 = \frac{1}{\sqrt{3}}$ and $C_3 = -\frac{1}{\sqrt{3}}$.

The atomic orbitals of the new energy states (i.e., sp_a^2, sp_b^2, and sp_c^2) are centered on the atom, separated by 120°, and directed toward the corners of an equilateral triangle as shown in Figure 3.4. These three orbitals have high electron probability, and three electrons of the same energy.

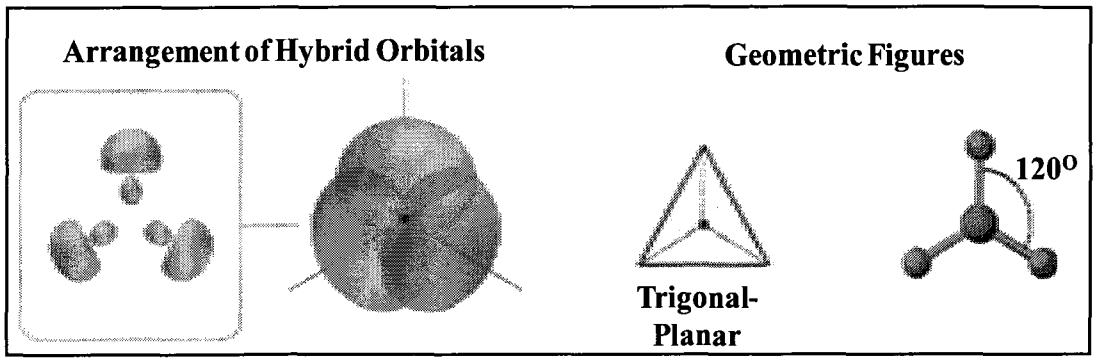

Figure 3.4 New atomic orbitals (i.e., $\mathbf{sp_a^2}$, $\mathbf{sp_b^2}$, and $\mathbf{sp_c^2}$) resulting from mixing the 2s orbital with two of the 2p orbitals ($2p_x$, $2p_y$, or $2p_z$). Source: www.chem.umass.edu[5].

3.4. sp^3 Hybrid Orbitals[1,2,3]

In the sp^3 orbital hybridization model the 2s orbital is hybridized or mixed with all three of the 2p orbitals ($2p_x$, $2p_y$, and $2p_z$), which results in four equivalent sp^3 orbitals as shown in Figure 3.5. Each sp^3 hybrid orbital consists of a large lobe, which points in one direction, and a small lobe, which points in the opposite direction as shown in Figure 3.6.

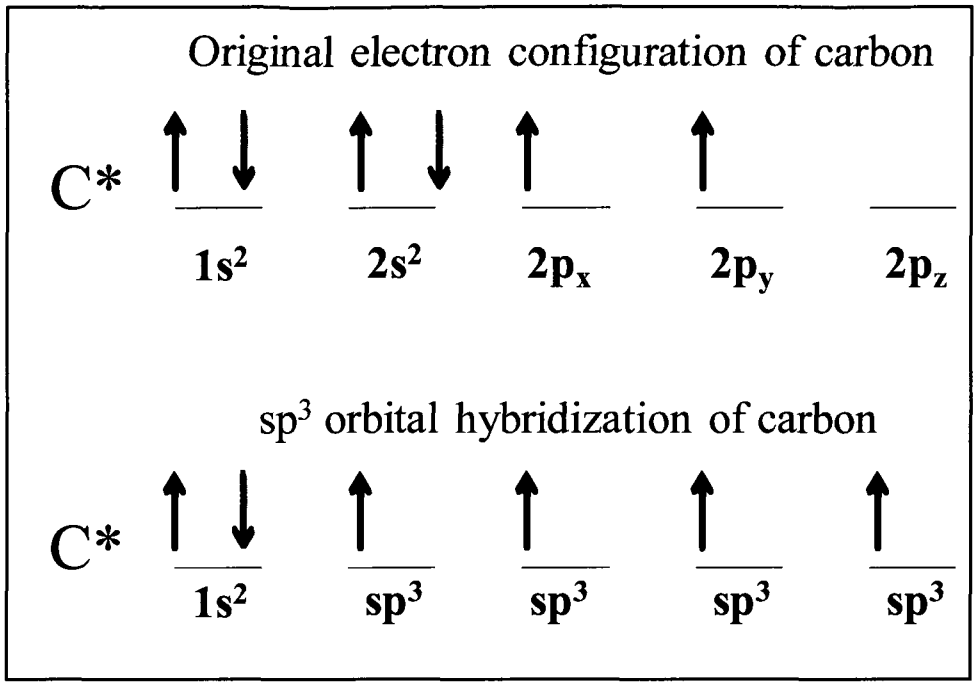

Figure 3.5 A hybridization model of sp^3 orbitals.

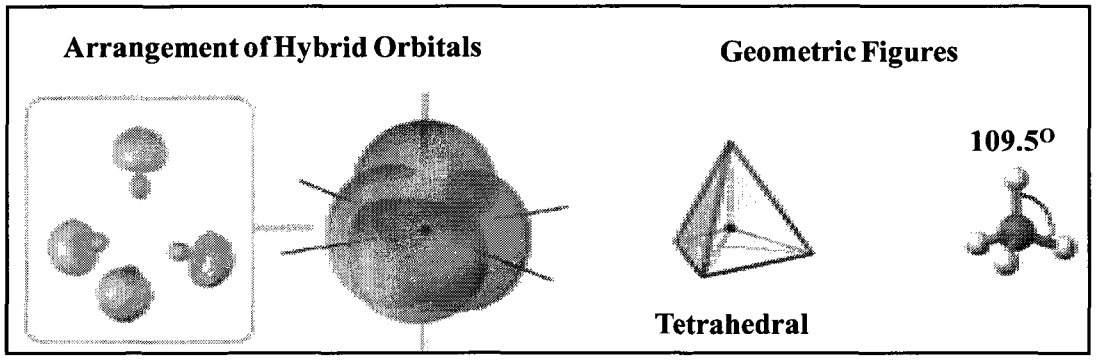

Figure 3.6 New atomic orbitals (i.e., $\mathbf{sp_a^3}$, $\mathbf{sp_b^3}$, $\mathbf{sp_c^3}$, and $\mathbf{sp_d^3}$) resulting from mixing the 2s orbital with the three 2p orbitals ($2p_X$, $2p_Y$, and $2p_Z$). Source: www.chem.umass.edu[5].

The tetrahedral bond directions from a carbon atom that is at the center can be selected as (1, 1, 1), (-1, -1, 1), (-1, 1, -1), or (1, -1, -1). The combination of the 2s and the three 2p atomic orbitals then can be mathematically represented by Equations 3.11, 3.12, 3.13, and 3.14.

$$|sp_a^3\rangle = \frac{1}{2}\left[|2s\rangle + |2p_x\rangle + |2p_y\rangle + |2p_z\rangle\right] \quad (3.11)$$

$$|sp_b^3\rangle = \frac{1}{2}\left[|2s\rangle - |2p_x\rangle - |2p_y\rangle + |2p_z\rangle\right] \quad (3.12)$$

$$|sp_c^3\rangle = \frac{1}{2}\left[|2s\rangle - |2p_x\rangle + |2p_y\rangle - |2p_z\rangle\right] \quad (3.13)$$

$$|sp_d^3\rangle = \frac{1}{2}\left[|2s\rangle + |2p_x\rangle - |2p_y\rangle - |2p_z\rangle\right] \quad (3.14)$$

The atomic orbitals of the new energy states (i.e., sp_a^3, sp_b^3, sp_c^3, and sp_d^3) are centered on the atom, separated by 109.5°, and directed toward the corners of a regular tetrahedron. These four orbitals have high electron probability, and four electrons of the same energy.

In general for sp^n hybridization, there are (n+1) electrons belonging to the hybridized σ orbital of the carbon atom, and [4 - (n+1)] electrons belonging to the π orbitals that originate from the unchanged p orbitals. In the case of sp^3 hybridization, four valance electrons occupy four σ bonding states. It is also possible for carbon atoms to have a mixed sp^2 and sp^3 character described as sp^{2+n} with $0 < n < 1$. This is the case for the pentagon rings found in fullerenes whose bonding is basically sp^2 but whose three-dimensional bending gives these carbon atoms a partially sp^3 character.

This can result in possible sp^2 hybridization of a planner carbon ring and hybridization found in fullerenes.

References

1. K. Vollhardt and N. Schore, Organic Chemistry: Structure and Function, (Oxford University Press, New York, NY, 2002).

2. R. Saito, G. Dresselhaus, and M. Dresselhaus, Physical Properties of Carbon Nanotubes, (Imperial College Press, Lomdpm, ON, Canada, 1999).

3. http://www.science.uwaterloo.ca/~cchieh/cact/c120/hybrid.html, February 2010.

4. A. Beiser, Perspectives of Modern physics, (McGraw-Hill, New York, NY, 1969).

5. http://www.chem.umass.edu, February 2010.

Chapter 4

Quantitative EELS Investigation of Carbon Materials

The atomistic and/or nanoscale properties that enable improved tribological performance of carbon onions have not yet been clearly identified. The potential properties, which might influence the frictional performance of these nano-materials, are: 1) the electronic interactions between individual nano-surfaces and/or with wear surfaces; 2) the individual nano-mechanical properties that affect collective load bearing; and 3) the effect of defects on these properties.

The focus of the present work is on the electronic interactions between individual nano-surfaces described by the sp^2 or sp^3 bond hybridization of the carbon onion surfaces. The sp^2/sp^3 bond hybridization ratio is an important fundamental tribological property because sp^2-sp^2 regions would be π-electron rich and able to slide like graphene layers, while sp^3-sp^3 regions could form chemical bonds leading to atomistic stiction.

For carbon onions, there is a known topographical evolution, which is observable by HRTEM, from a spherical to a polyhedral multi-layer structure as a function of increasing synthesis temperature[1]. It has been postulated that the structural evolution is accompanied by a change of the sp^2/sp^3 bond hybridization ratio[2]. However, this has not been quantitatively investigated in the carbon onion nanomaterial system. In this research, the postulated correlation of the sp^2/sp^3 bond hybridization ratio with the

spherical to polyhedral structural evolution is quantitatively investigated using EELS due to its high spatial resolution (~1 eV) and sensitivity to different bond structures within a sample[3].

4.1. Quantitative Method: EELS

EELS is a sensitive analytical method that can measure a transition edge (inner shell to conduction band) rather than a Gaussian transition distribution[3]. As discussed in Chapter 2, there are several transition edges: K, L, and M, defined by the atomic shell that an ejected electron originates from. The present work utilizes the K-shell transition of a carbon 1s electron to an available conduction band (*) energy level. As discussed in Chapter 3, the available conduction band energy levels in an sp^2 hybridized system are the π^* and the σ^* levels. Therefore, the expected K-edges for a purely sp^2 carbon nanomaterial are the $1s \rightarrow \pi^*$ and the $1s \rightarrow \sigma^*$ transition edges. Figure 4.1 shows a typical EELS spectrum from a largely sp^2 carbon onion sample with the transition edges marked. Each leading edge is actually a delta function, which is symmetrically broadened by the energy resolution of the instrument.

A purely sp^2 material would have a ratio of intensities $I_{1s \rightarrow \pi^*} / I_{1s \rightarrow \sigma^*} =$ 1/3 because there are three sp^2 hybridized σ^* energy levels for every one π^* unhybridized energy level. A departure from this ratio means that the material is not purely sp^2. In quantitative EELS, the integrated areas under the carbon K-ionization transition edges are used to experimentally determine any departure of a test sample (U) from a known sp^2

reference sample (R) (i.e., $\% \ sp^2 \approx \frac{I_\pi^U / I_\sigma^U}{I_\pi^R / I_\sigma^R}$). However, there are several research issues involved in the quantitative EELS measurement, which are discussed next.

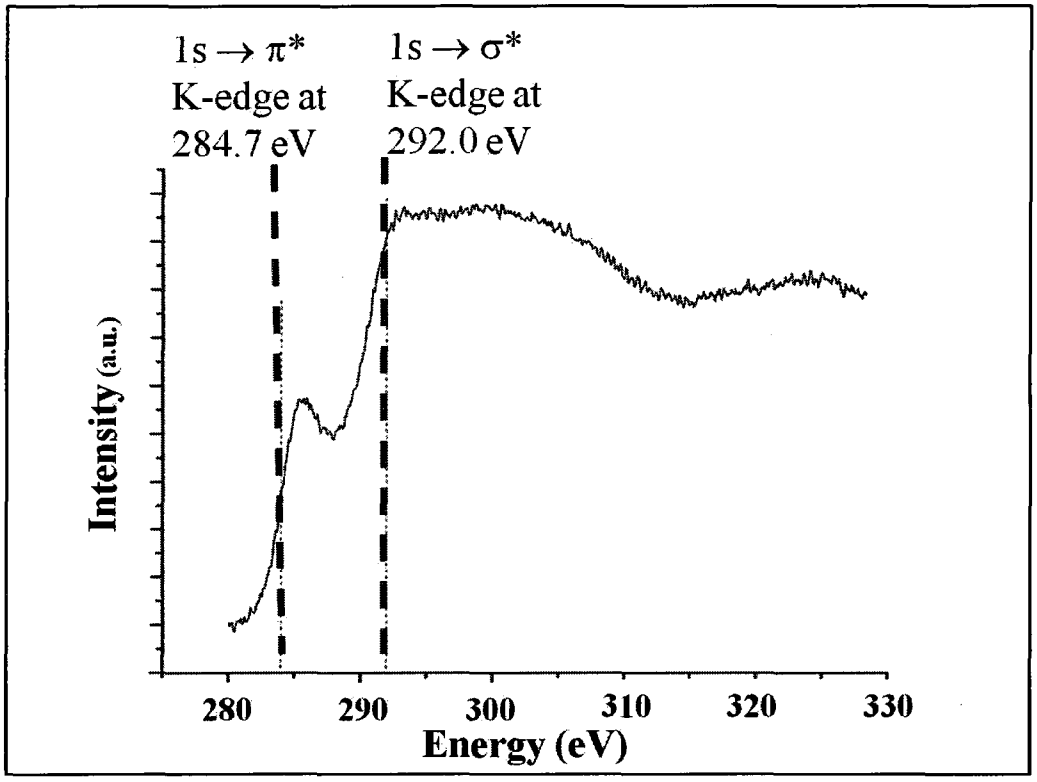

Figure 4.1 A typical EELS spectrum from a largely sp^2 carbon onion sample, synthesized at 1700°C, with the transition edges marked.

4.2. Quantitative EELS: Research Issues

4.2.1. Near-Edge Segregation

To precisely characterize the sp^2/sp^3 content using EELS, the π^* feature and its cross section must be isolated from the spectrum. Typical π^* and σ^* peak segregation methods have accuracy limitations due to the assumption that these features are well

separated in energy, and their cross sections can be independently obtained. However, the spectrum edge intensities can be changed by the plural inelastic scattering and plasmon (low-energy) losses (discussed in Chapter 2) that can shift the oscillator strengths to higher or lower energies[4]. Figure 4.2, shown below, is adapted from a theoretical calculation of the energy-loss-near-edge structure (ELNES) for graphite, which is a purely sp^2 material[4]. It makes the point that both the $1s \rightarrow \pi^*$ and the $1s \rightarrow \sigma^*$ transitions have long tails and therefore significant overlap out to high energies. Although only two transitions are involved, clear segregation of the $1s \rightarrow \pi^*$ and the $1s \rightarrow \sigma^*$ components is problematic if using an energy window or functional fitting method that does not accurately take the higher energy contributions into account.

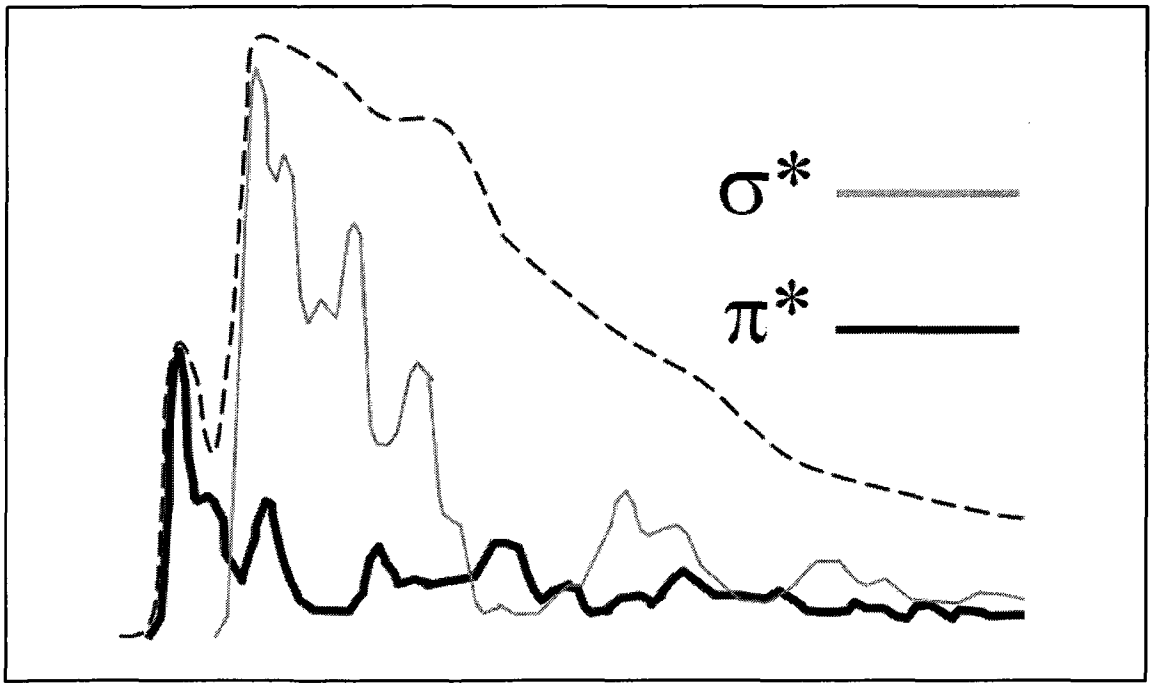

Figure 4.2 A theoretical calculation of the energy-loss-near-edge structure (ELNES) for a purely sp^2 graphite.

4.2.2. sp^2 Reference Samples

Graphite and C_{60} are both used as sp^2 reference (R) samples in quantitative EELS of carbon materials or nanomaterials. Both have properties which cause them to deviate from an ideal purely sp^2 standard. Graphite, typically highly oriented pyrolytic graphite (HOPG), is a directional material with different electronic properties in its a-axis and c-axis orientations. Previous research has demonstrated that this affects its interaction with the TEM electron beam[5]. The strongest effect is on the interaction of the π^* electrons with beam, which changes the integrated area under the $1s \rightarrow \pi^*$ spectral curve. The minimum integrated $1s \rightarrow \pi^*$ area is found when the electron beam is parallel to the HOPG c-axis, a configuration referred to as the "magic angle". The theoretical near edge π^* and σ^* spectra, shown in Figure 4.2, were from an orientation resolved calculation, in which the graphite sample and the electron beam were at the "magic angle" during the Monte Carlo investigation[4,5].

A C_{60} fullerene reference sample does not have the same strong orientation dependence as a graphite sample because the π^* energy levels are spatially randomized by the spherical structure. C_{60} does have bond hybridization character of $sp^{2.28}$ rather than sp^2 due to its tight curvature[4]. However, the curvature influence affects the $1s \rightarrow \pi^*$ and $1s \rightarrow \sigma^*$ integrated area about equally[6], rather than preferentially affecting the $1s \rightarrow \pi^*$ integrated area. A C_{60} fullerene reference sample is used in the present work.

4.2.3. Inclusion of the 287.0 eV Peak

The most extensive literature on quantitative EELS of carbon materials is for the amorphous tetrahedral carbon (a-C) system. The sp^2/sp^3 ratio is an important fundamental measurement in the a-C system, although by reason of its correlation with hardness rather than low friction.

Investigation of the hybridized chemical bonding of a-C samples revealed the two major sp^2 carbon edges in the EELS spectra. The first edge of the carbon K-edge spectra corresponds to the $1s \rightarrow \pi^*$ transition at 284.7 eV, and the second prominent edge corresponds to the $1s \rightarrow \sigma^*$ transition at 292.0 eV. The inclusion of an intermediate peak at about 287.0 eV has been a subject of discussion. The interpretation of the feature at 287.0 eV has been variously interpreted as a peak due to a C-H electronic transition[7], a peak due to an electronic transition within a "pseudo-molecular" carbon domain embedded within an a-C matrix[8], and as part of the $1s \rightarrow \pi^*$ edge transition itself[4]. In the present research, the temperature evolution of the carbon onion system was used to test the need for a separate 287.0 eV peak.

4.3. EELS Deconvolution Techniques

4.3.1. Two-Energy Windows Method

The two-energy windows method is a simple technique used to characterize the sp^2/sp^3 content within a carbon sample. In this method, two-energy windows (ΔE_π and ΔE_σ) are arbitrarily selected and placed at points in the EELS spectrum that appear to represent the separation of the $1s \rightarrow \pi^*$ from the $1s \rightarrow \sigma^*$ transition. For example, a typical energy window selection is 282-288 eV for the $1s \rightarrow \pi^*$ and 284-310 eV for the

$1s \rightarrow \sigma^*$. These choices are based on the assumption that the transition can be completely separated from the σ^* transition. Then, the integrated areas of both energy windows are determined, and their ratio is compared with a reference ratio to deduce the sp^2 or sp^3 percentage. This technique strongly depends on the selection of the widths of both energy windows, and it can result in an uncertainty of about 10% in the sp^2/sp^3 ratio[4].

4.3.2. Functional Fitting Method

The functional fitting method is another technique that uses different distribution functions to deconvolve the EELS spectrum. In this technique, two or three peaks are typically utilized to deconvolve the carbon EELS spectrum. The lowest fitted curve at about 285.0 eV corresponds to the π^* feature, and the highest fitted curve at about 8 eV above the π^* onset corresponds to the σ^* feature. The inclusion of a third intermediate fitted curve at about 287.0-288.0 eV is an area of discussion. To determine the sp^2 fraction in a carbon sample using this technique, the integrated areas of the fitted edges are calculated and compared with a reference ratio to deduce the sp^2 percentage as given by Equation 4.1[8,9],

$$\% \, sp^2 \approx \frac{I_\pi^U / I_\sigma^U}{I_\pi^R / I_\sigma^R}, \tag{4.1}$$

where I_π^U is the integrated area under the fitted curve corresponding to the π^* transition of the unknown material, I_σ^U is the integrated area under the fitted curve corresponding to

the σ* transition of the unknown material, I_{π}^{R} is the integrated area under the fitted curve corresponding to the π* transition of the reference material, and I_{σ}^{R} is the integrated area under the fitted curve corresponding to the σ* transition of the reference material. The sp^3 fraction in the sample can be determined by subtracting the sp^2 percentage from 100% (i.e., $\%sp^3 = 100\% - \%sp^2$). The sp^2/sp^3 ratio can be then calculated by dividing the sp^2 fraction by the sp^3 fraction (i.e., sp^2/sp^3 ratio $= \left(\frac{\%sp^2}{\%sp^3}\right)$[9].

The functional fitting method again makes the assumption that the π* and σ* transitions can be completely separated. Also, all the examples reviewed in this research used symmetric Gaussian or Lorentzian functions to fit the spectral data within a typical 282-310 eV total energy range. This results in over-representation of the near edge contributions and under-representation of the higher-order tail.

4.4. Discussion of Issues and a New Approach

The two-energy window and the functional fitting methods both make the assumption that the π* transition can be separated from the σ* transition within the near-edge 282-310 eV region. Functional fitting methods also rely on 2- or 3-peak deconvolution using symmetric Gaussian and Lorentzian functions over the same energy range. While these functions accurately reproduce the instrumentally broadened delta function edge, they do not effectively represent the higher energy oscillator strengths of the 1s → π* and 1s → σ* transitions.

One solution is to represent the higher energy contributions with a large number of additional Gaussian or Lorentzian peaks, then sum them appropriately to represent the $1s \rightarrow \pi^*$ and $1s \rightarrow \sigma^*$ transitions. It would be difficult to identify which peaks belong with which transition. A new approach in this thesis is to use a fitting function that can more accurately reproduce the higher energy asymmetric transition characteristics.

References

1. S. Tomita, T. Sakurai, H. Ohta, M. Fujii, and S. Hayashi, "Structure and electronic properties of carbon onions", The Journal of Chemical Physics **114**: 7477 (2001).

2. S. Tomita, M. Fujii, S. Hayashi, and K. Yamamoto, "Electron energy-loss spectroscopy of carbon onions", Chemical Physics Letters **305**: 225-229 (1999).

3. C. Brundle, C. Evans, and S. Wilson, "Encyclopedia of Materials Characterization", Butterworth-Heinemann, Stoneham, MA (1992).

4. J. Titantah, and D. Lamoen, "Technique for the sp^2/sp^3 characterization of carbon materials: Ab initio calculation of near-edge structure in electron-energy-loss spectra", Physical. Review B **70**, 075115 (2004).

5. A. Papworth, C. Kiely, A. Burden, S. Silva, and G. Amaratunga, "Electron-energy-loss spectroscopy characterization of the sp2 bonding fraction within carbon thin films", Physical Review B **62**: 12628–12631 (2000).

6. J. Martins, N. Troullier and J.Weaver, "Analysis of occupied and empty electronic states of C_{60}", Chemical Physics letters **180**: 457-460 (1991).

7. Mykhaylyka, Y. Solonin, D. Batchelder, and R. Brydson, "Transformation of nanodiamond into carbon onions: A comparative study by high-resolution transmission electron microscopy, electron energy-loss spectroscopy, x-ray diffraction, small-angle x-ray scattering, and ultraviolet Raman spectroscopy", Journal of Applied Physics **97**: 074302 (2005).

8. R. Brydson, Z. Zhili, and A. Brown, "Revisiting the determination of carbon sp^2/sp^3 ratios of the EELS carbon K-edge", EMC 2008 14th European Microscopy Congress **1**: 357-358 (2008).

9. S. Osswald, G. Yushin, V. Mochalin, S. O. Kucheyev, and Y. Gogotsi, "Control of sp^3/sp^2 carbon ratio and surface chemistry of nanodiamond powders by selective oxidation in air", Journal of American Chemical Society, **128**: 11635-11642 (2006).

Chapter 5

Quantitative EELS Investigation of Carbon Onions

All of the considerations in the previous chapter had to be separately considered in order to perform the quantitative EELS investigation of the new carbon onion system that is one of the main contributions of this thesis. In this research, different functional fitting techniques were utilized to precisely reproduce the characteristics of the leading edge, which is a delta function symmetrically broadened by the energy resolution of the instrument, and the higher energy states, which are the asymmetric contributions from all available energy levels in the energy density of states[1]. The techniques, used in this thesis to analyze the EELS spectrums of carbon onions, represent a new research approach for the carbon onion system and for carbon nanomaterials.

The EELS investigation is set within the context of HRTEM and SEM experiments that correlate the fundamental electronic sp^2/sp^3 investigations with the synthesis conditions.

5.1. Structural Characterization Using HRTEM

HRTEM images confirmed that the previously reported[2] spherical to polygonal structural transition occurs over a temperature range of 1700°C to 2300°C for the present synthesis conditions. No evidence for a remnant NCD core was observed in the carbon

onion samples. Therefore, the HRTEM images indicated that the NCD starting material, shown in Figure 5.1, had been completely converted into the innermost carbon onion layers. Representative images of the spherical to polygonal structural transition are shown in Figure 5.2 (a-c).

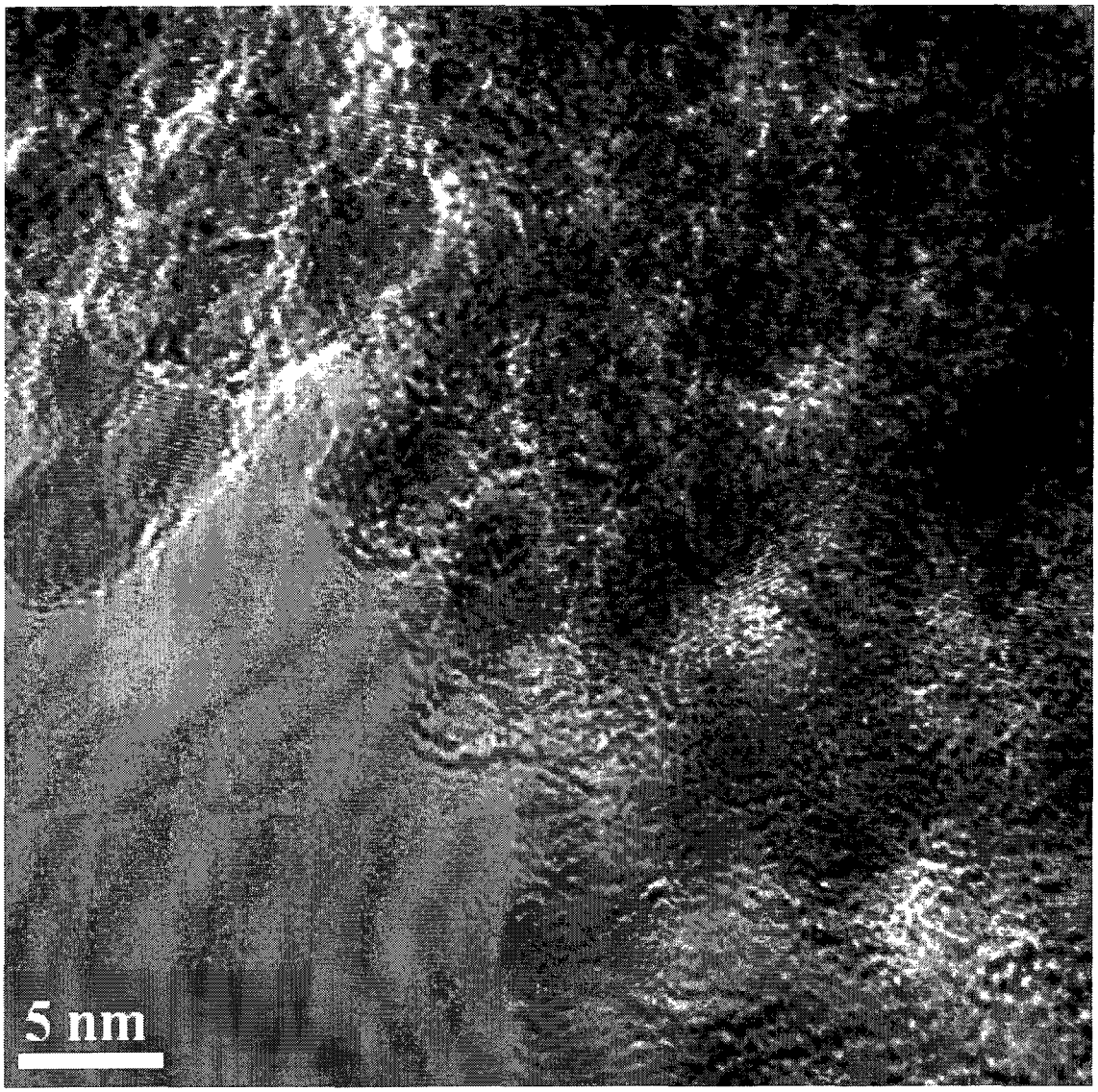

Figure 5.1 An HRTEM image of the largely sp^3 NCD. Image by: Raied A. Al-Duhileb.

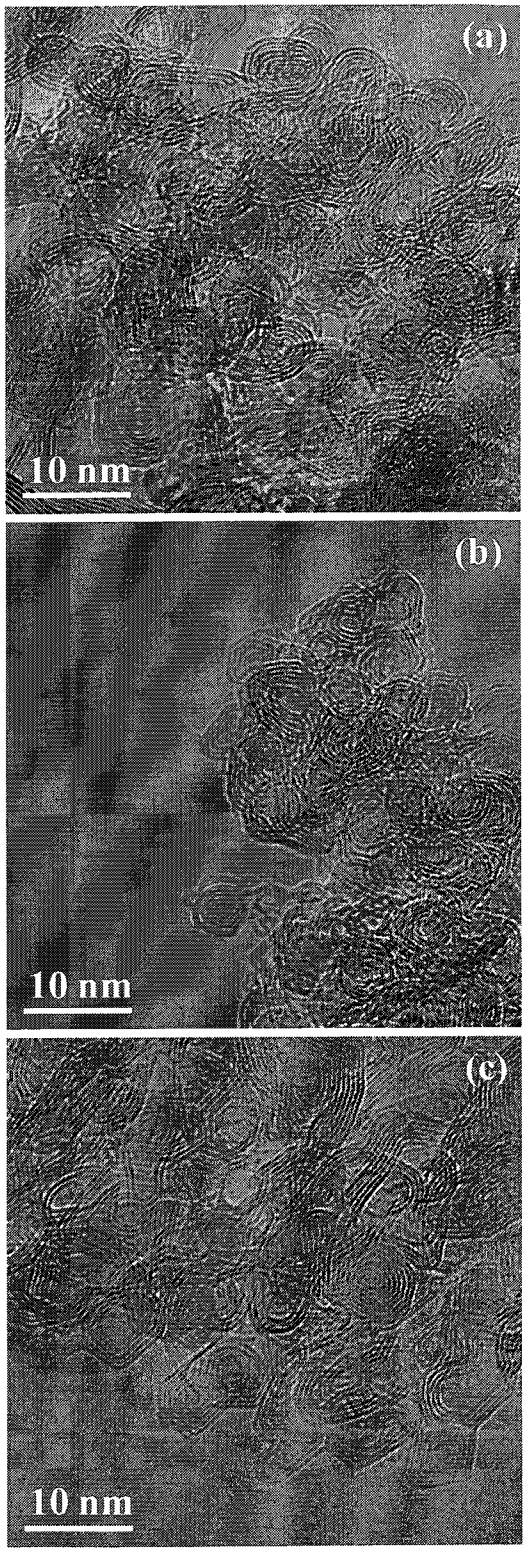

Figure 5.2 HRTEM images of the structural transition from spherical to polygonal for carbon onions synthesized at temperatures (a) 1700°C (b) 2000°C and (c) 2300°C. Images by: Raied A. Al-Duhileb.

For quantitative EELS analysis, C_{60} fullerenes were used as a non-directional[3] reference standard having a theoretical intensity ratio (i.e., $I_{\pi}^{R}/I_{\sigma}^{R}$) of one-third. A group of C_{60} fullerenes suspended over the edge of a lacey film hole is shown in Figure 5.3. The individual cages are difficult to distinguish due to light contrast and small size; therefore, care was taken to investigate only groups suspended well over the edge of a lacey film hole.

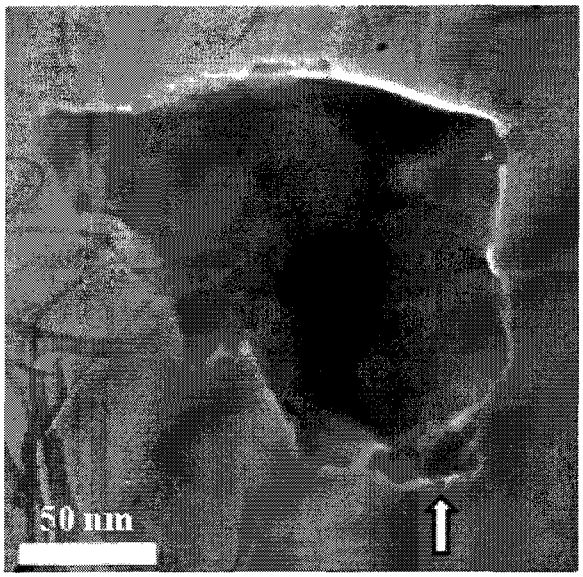

Figure 5.3 A TEM image showing aggregate C_{60} particles suspended over a lacey film hole. Image by: Raied A. Al-Duhileb.

In the coming sections, we quantitatively measure the sp^2/sp^3 bond hybridization ratio of different carbon onion samples prepared at an increasing synthesis temperature using several EELS deconvolution techniques. We also investigate (a) whether inclusion of a 287.0 eV feature is required in a 2-peak fit by a symmetrical deconvolution function; and (b) whether inclusion of a 287.0 eV feature in a 3-peak fit by a symmetrical deconvolution function produces a good fit.

5.2. EELS Deconvolution: Gaussian Function

Approach 1 (Gaussian function with 2-peak fitting):

The core loss EELS spectrums of carbon onions, prepared at increasing synthesis temperature, were analyzed using symmetric Gaussian area deconvolution function:

$$y = \frac{a_0}{\sqrt{2\pi a_2}} \exp\left[-\frac{1}{2}\left(\frac{x - a_1}{a_2}\right)^2\right], \tag{5.1}$$

where a_0 is the area, a_1 if the center, and a_2 is the width.

The results, which were obtained using 2-peak fitting, are shown in Table 5.1. A typical deconvolution using this method is shown in Figure 5.4. No clear increasing or decreasing sp^2/sp^3 trend was observed using a Gaussian function with 2-peak fitting (Figure 5.5). Furthermore, in at least one instance (row identified with bold border), a 3-peak fit that included a peak at about 287.0 eV was required to obtain a 0.989 coefficient of determination (CoD).

Table 5.1 sp^2/sp^3 ratio of carbon onion samples prepared at increasing synthesis temperature. The results were obtained using Gaussian deconvolution and 2-peak fit.

Temp.	CoD	I_π	I_σ	$\%sp^2$	$\%sp^3$	sp^2/sp^3
1700°C	0.998	28384.32	106570.00	0.64	0.36	1.76
1700°C	0.989	38044.33	160220.00	0.85	0.15	5.56
2000°C	0.992	64570.15	359260.00	0.46	0.54	0.86
2000°C	0.997	81883.80	484740.00	0.44	0.56	0.78
2000°C	0.998	288310.00	813370.00	0.99	0.01	99.00
2300°C	0.998	114530.00	419090.00	0.65	0.35	1.86
2300°C	0.993	142900.00	565360.00	0.61	0.39	1.57

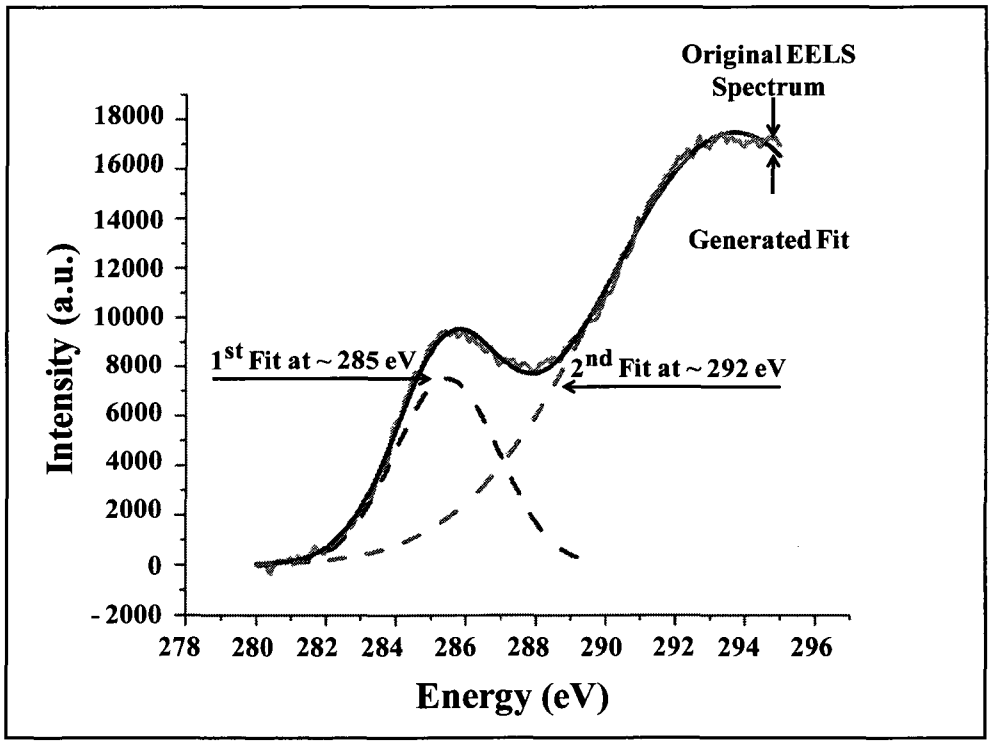

Figure 5.4 Deconvolution of the core loss EELS spectrum of carbon onions, prepared at 1700°C. The original spectrum was deconvolved using 2-peak fit and the symmetric Gaussian deconvolution.

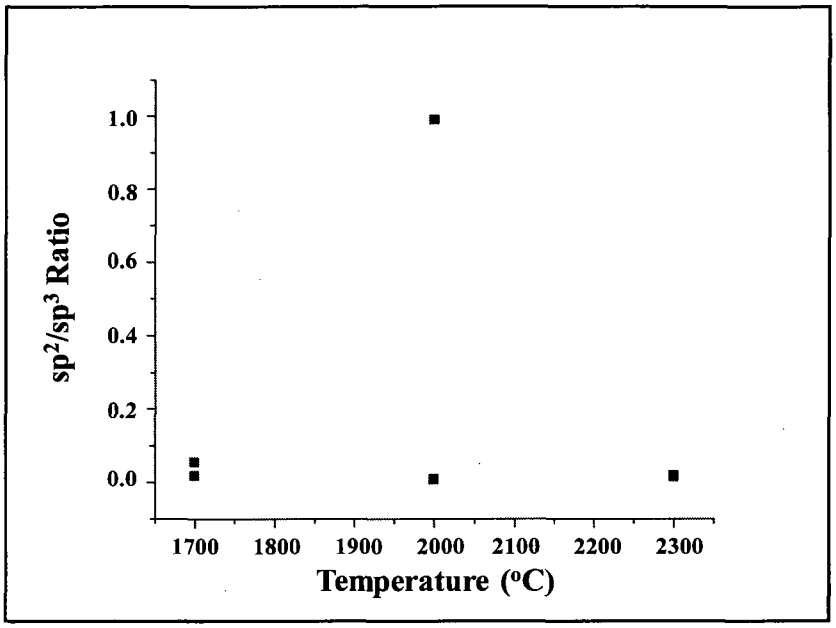

Figure 5.5 A plot of the sp^2/sp^3 ratio in carbon onions as a function of synthesis temperature. The plot is based on results obtained using 2-peak fit and the symmetric Gaussian deconvolution.

Approach 2 (Gaussian function with 3-peak fitting):

The results of 3-peak fitting using symmetric Gaussian deconvolution with inclusion of a third feature at 287.0 eV (rows identified with bold borders) are shown in Table 5.2. A typical deconvolution using this method is shown in Figure 5.6. Although all samples had CoD of 0.97 or above using the 3-peak symmetric fit, no clear increasing or decreasing sp^2/sp^3 trend was observed (Figure 5.7) for the Gaussian deconvolution with 3-peak fitting.

Table 5.2 sp^2/sp^3 ratio of carbon onion samples prepared at increasing synthesis temperature. The results were obtained using Gaussian deconvolution and 3-peak fit.

Temp.	CoD	I_π	I_σ	$\%sp^2$	$\%sp^3$	sp^2/sp^3
1700°C	0.990	23974.79	32161.78	2.22	-1.22	-1.82
1700°C	0.981	45052.71	22508.18	2.27	-1.27	-1.79
2000°C	0.974	67397.28	81505.44	1.96	-0.96	-2.04
2000°C	0.995	109060.00	36756.27	2.42	-1.42	-1.70
2000°C	0.999	256560.00	58267.76	0.99	0.01	99.00
2300°C	1.000	92994.61	27554.33	2.47	-1.47	-1.68
2300°C	0.993	133940.00	38433.95	2.48	-1.48	-1.68

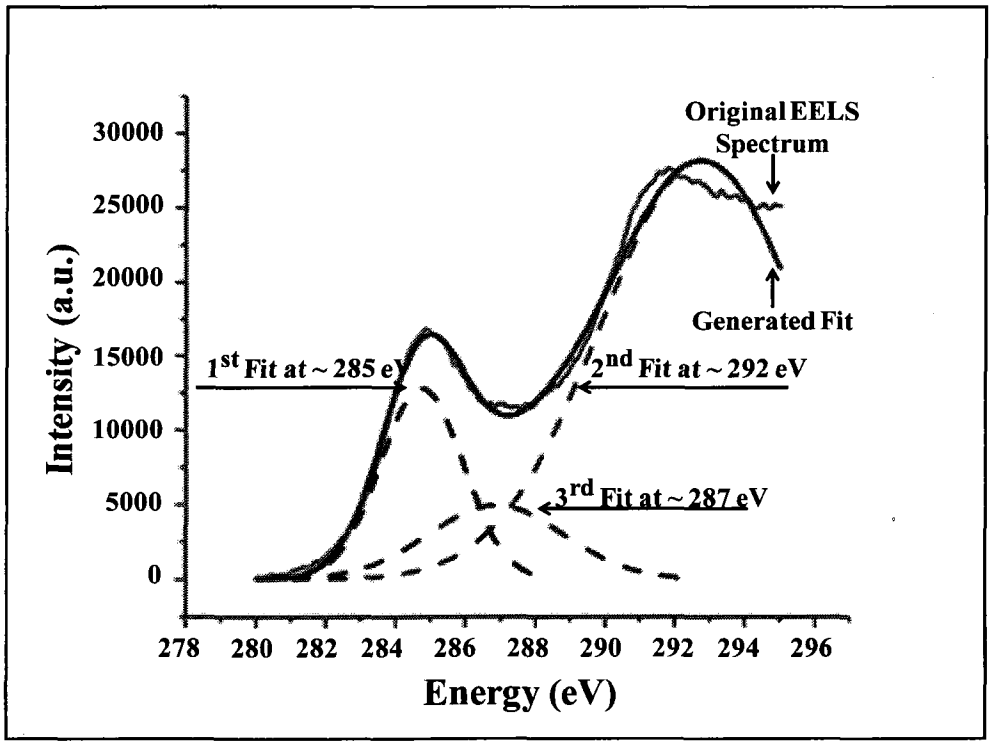

Figure 5.6 Deconvolution of the core loss EELS spectrum of carbon onions, prepared at 1700°C. The original spectrum was deconvolved using 3-peak fit and the symmetric

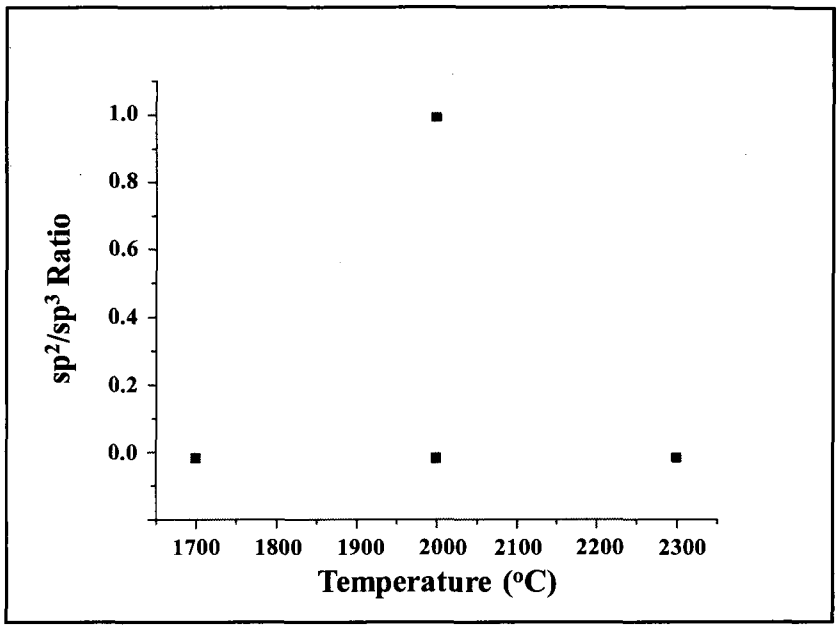

Figure 5.7 A plot of the sp^2/sp^3 ratio in carbon onions as a function of synthesis temperature. The plot is based on results obtained using 3-peak fit and the symmetric Gaussian deconvolution.

5.3. EELS Deconvolution: Lorentzian Function

Approach 1 (Lorentzian area function with fixed starting and end points):

To represent the experimental data, a 3-peak functional fitting was performed using symmetric Lorentzian area function:

$$y = \frac{a_0}{\pi a_2 \left[1+\left(\frac{x-a_1}{a_2}\right)^2\right]}, \tag{5.2}$$

where a_0 is the area, a_1 if the center, and a_2 is the width.

Two appropriately placed peaks represented the π^* and σ^* edges, and a third peak at 287.0 eV was included. The results of the three-peak Lorentzian deconvolution are

shown in table 5.3. A typical deconvolution using this approach is shown in Figure 5.8. The results had a coefficient of determination (CoD) of 0.95 or above. The data in each temperature displayed a range of values, and no clear increasing or decreasing sp^2/sp^3 trend was observed (Figure 5.9).

Table 5.3 sp^2/sp^3 ratio of carbon onion samples prepared at increasing synthesis temperature. The results were obtained using symmetric Lorentzian area deconvolution with 3-peak fit and fixed starting & end points.

Temp.	CoD	I_π	I_σ	$\%sp^2$	$\%sp^3$	sp^2/sp^3
1700°C	0.976	16163.17	114220.00	0.53	0.47	1.13
1700°C	0.970	26625.66	194910.00	0.45	0.55	0.81
2000°C	0.961	44847.17	379460.00	0.35	0.65	0.55
2000°C	0.952	75468.82	490150.00	0.42	0.58	0.72
2000°C	0.982	112210.00	904160.00	0.60	0.40	1.51
2300°C	0.954	57657.10	447680.00	0.50	0.50	0.99
2300°C	0.961	72822.98	616480.00	0.43	0.57	0.75

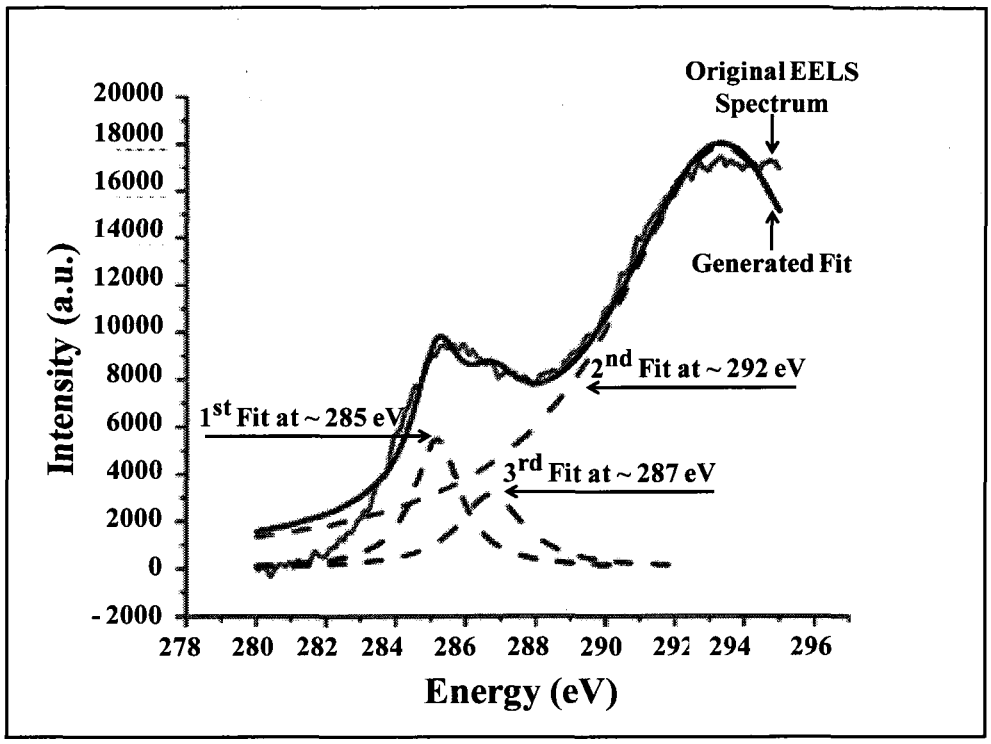

Figure 5.8 Deconvolution of the core loss EELS spectrum of carbon onions, prepared at 1700°C. The original spectrum was deconvolved using 3-peak fit and the symmetric Lorentzian area deconvolution.

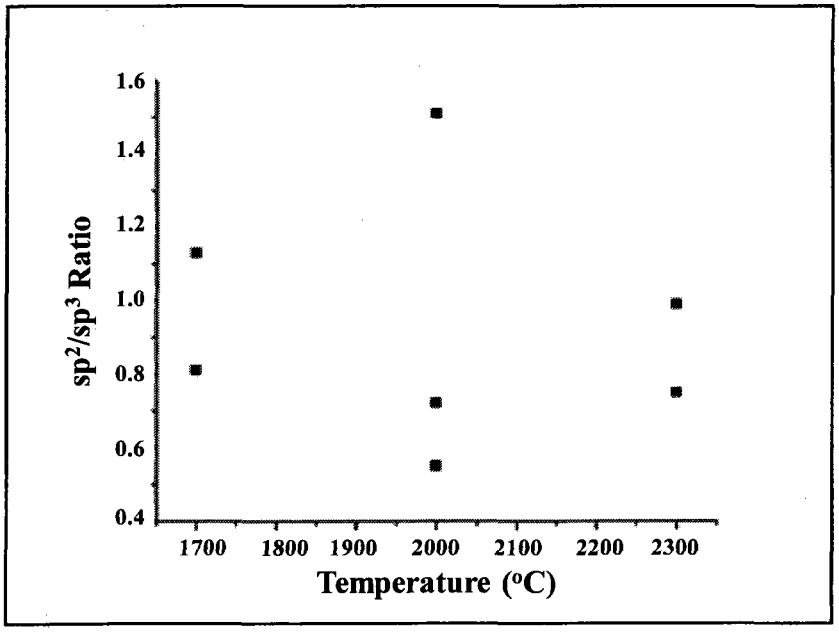

Figure 5.9 A plot of the sp^2/sp^3 ratio in carbon onions as a function of synthesis temperature. The plot is based on results obtained using approach 1.

Approach 2 (Lorentzian area function with exact inflection points):

The π^* and σ^* edges were located within about ±2 eV by using the inflection points within the appropriate π^* and σ^* data ranges to identify an edge. The start of the functional fit for the π^* transition was consistently set at 5 eV below the π^* edge identified by its inflection point. The finish of the functional fit for the σ^* transition was consistently set at 5 eV above the σ^* edge identified by its inflection point. The goal was to compensate for the observed overall shifting of the experimental data due to the zero-loss peak being not precisely set at zero. The inflection points and their differences are shown in Table 5.4. The differences fall in an expected 6-7 eV range. The results of the three-peak Lorentzian deconvolution are shown in Table 5.5

The data in each temperature displayed a range of values, and no clear increasing or decreasing sp^2/sp^3 trend was observed as shown in Figure 5.10.

Table 5.4 First and second inflection points (IPs) and their corresponding differences.

Temp.	1st IP	2nd IP	Δ (IPs)	Fit Start	Fit Finish
1700°C	283.90 eV	290.44 eV	6.54 eV	279 eV	295 eV
1700°C	283.96 eV	289.98 eV	6.02 eV	279 eV	295 eV
2000°C	278.94 eV	286.10 eV	7.16 eV	274 eV	291 eV
2000°C	283.42 eV	289.58 eV	6.16 eV	278 eV	295 eV
2000°C	283.16 eV	289.70 eV	6.54 eV	278 eV	295 eV
2300°C	280.23 eV	287.66 eV	7.43 eV	275 eV	293 eV
2300°C	283.86 eV	290.37 eV	6.51 eV	279 eV	295 eV

Table 5.5 sp^2/sp^3 ratio of carbon onion samples prepared at increasing synthesis temperature. The results were obtained using symmetric Lorentzian area deconvolution with 3-peak fit and exact inflection points.

Temp.	CoD	I_π	I_σ	$\%sp^2$	$\%sp^3$	sp^2/sp^3
1700°C	0.957	14822.24	113550.00	0.46	0.54	0.86
1700°C	0.962	29665.54	190820.00	0.47	0.53	0.88
2000°C	0.961	46691.33	381880.00	0.38	0.62	0.61
2000°C	0.942	72458.07	485390.00	0.44	0.56	0.80
2000°C	0.975	217300.00	862270.00	0.72	0.28	2.54
2300°C	0.967	77822.95	438060.00	0.60	0.40	1.51
2300°C	0.961	89663.65	614300.00	0.47	0.53	0.89

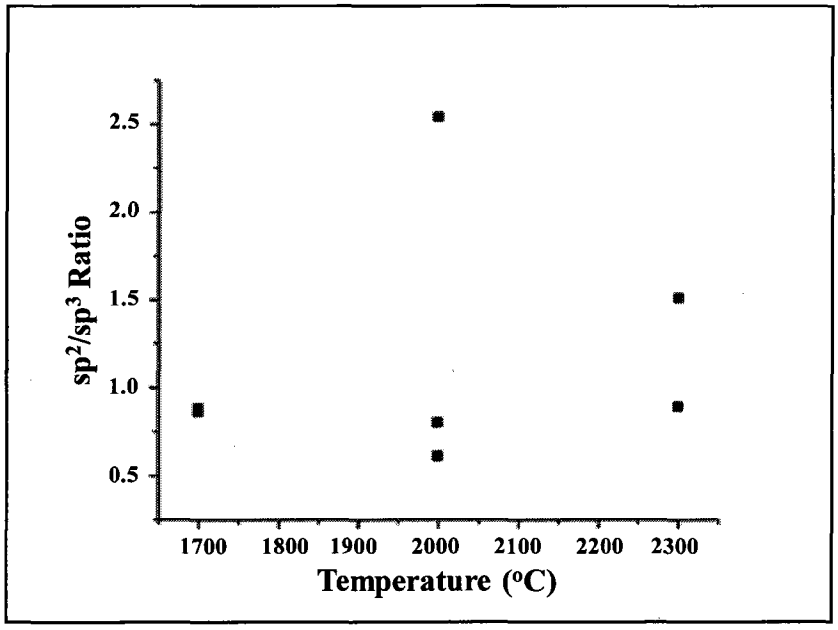

Figure 5.10 A plot of the sp^2/sp^3 ratio in carbon onions as a function of synthesis temperature. The plot is based on results obtained using approach 2.

5.4. EELS Deconvolution: F-Variance Function

The core loss EELS spectrums of carbon onion samples, prepared at increasing synthesis temperature, were deconvolved using an asymmetric f-variance deconvolution function:

$$y = \frac{a_0 \Gamma\left[\frac{a_3 + a_4}{2}\right]\left[\frac{a_3}{a_4}\right]^{\frac{a_3}{2}}\left[\frac{x - a_1}{a_2} + \frac{a_4 (a_3 - 2)}{a_3 (a_4 + 2)}\right]^{\frac{a_3}{2} - 1}}{a_2 \Gamma\left[\frac{a_3}{2}\right]\Gamma\left[\frac{a_4}{2}\right]\left[1 + \frac{a_3\left(\frac{x - a_1}{a_2} + \frac{a_4 (a_3 - 2)}{a_3 (a_4 + 2)}\right)}{a_4}\right]^{\frac{a_3 - a_4}{2}}}, \quad (5.2)$$

where a_0 is the area, a_1 if the center, a_2 is the width, a_3 is shape 1, and a4 is shape $_2$. As shown in Figure 5.11, the f-variance area function can accurately represent both the leading edges and higher energy contributions of the $1s \rightarrow \pi^*$ and $1s \rightarrow \sigma^*$ transitions.

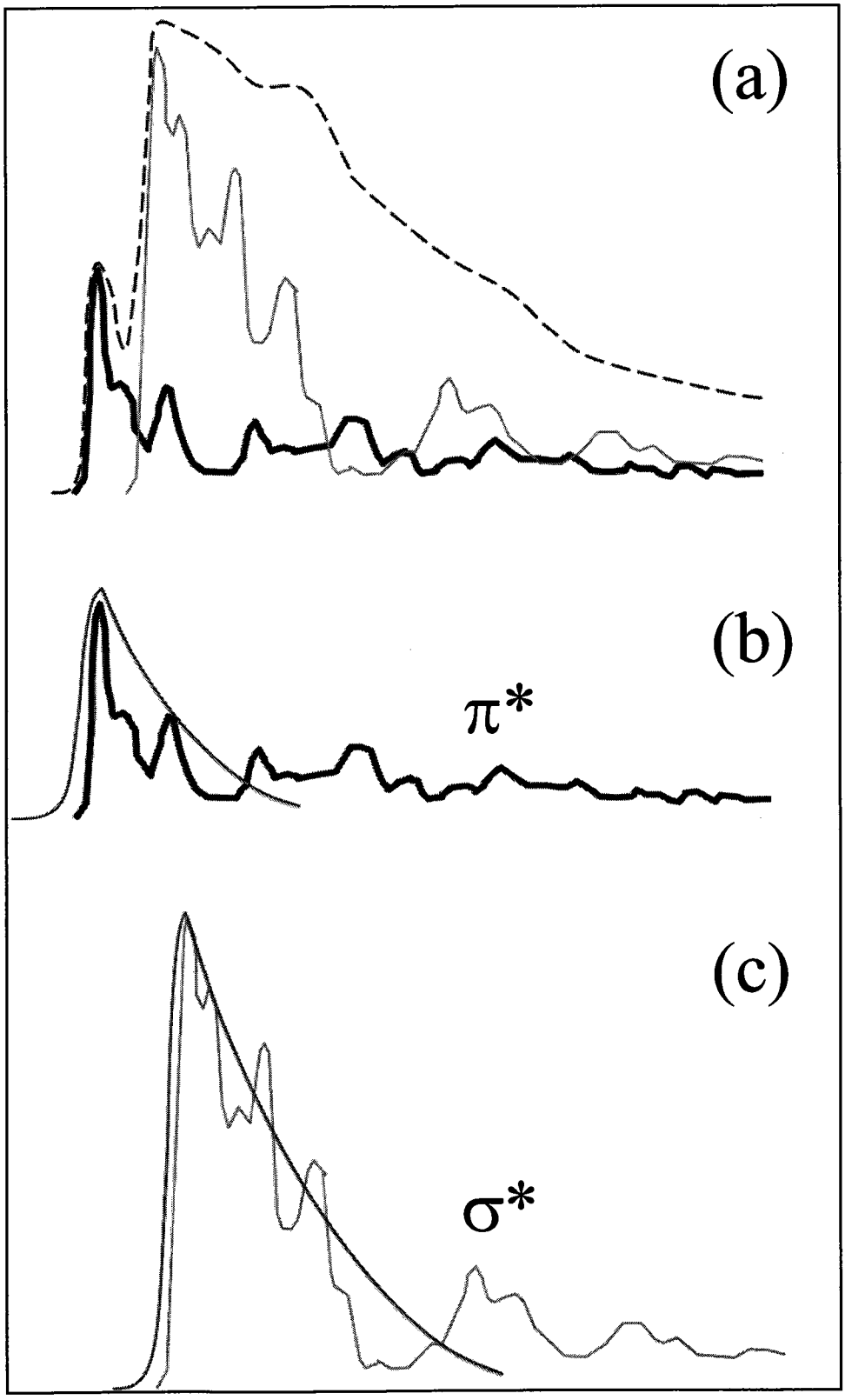

Figure 5.11 Theoretical near edge π* and σ* spectra from an orientation resolved calculation, in which a graphite sample and the electron beam were at the "magic angle".

The results, which were obtained using this method with 2-peak fitting, are shown in Table 5.6. A typical deconvolution using this method is shown in Figure 5.12. The results had a 0.97 CoD or above, and showed a clear trend, which was an increase in the sp^2/sp^3 bond hybridization ratio as shown in Figure 5.13.

Table 5.6 sp^2/sp^3 ratio of carbon onion samples prepared at increasing synthesis temperature. The results were obtained using asymmetric f-variance area deconvolution and 2-peak fit.

Temp.	CoD	I_π	I_σ	$\%sp^2$	$\%sp^3$	sp^2/sp^3
1700°C	0.999	39547.39	95377.24	0.89	0.11	7.94
1700°C	0.993	65823.27	156490.00	0.90	0.10	8.73
2000°C	0.978	117590.00	295790.00	0.86	0.14	6.25
2000°C	0.998	125260.00	437990.00	0.67	0.33	2.07
2000°C	0.997	369690.00	728380.00	0.99	0.01	99.00
2300°C	0.999	166230.00	358740.00	0.96	0.04	23.71
2300°C	0.996	225710.00	479510.00	0.97	0.03	32.19

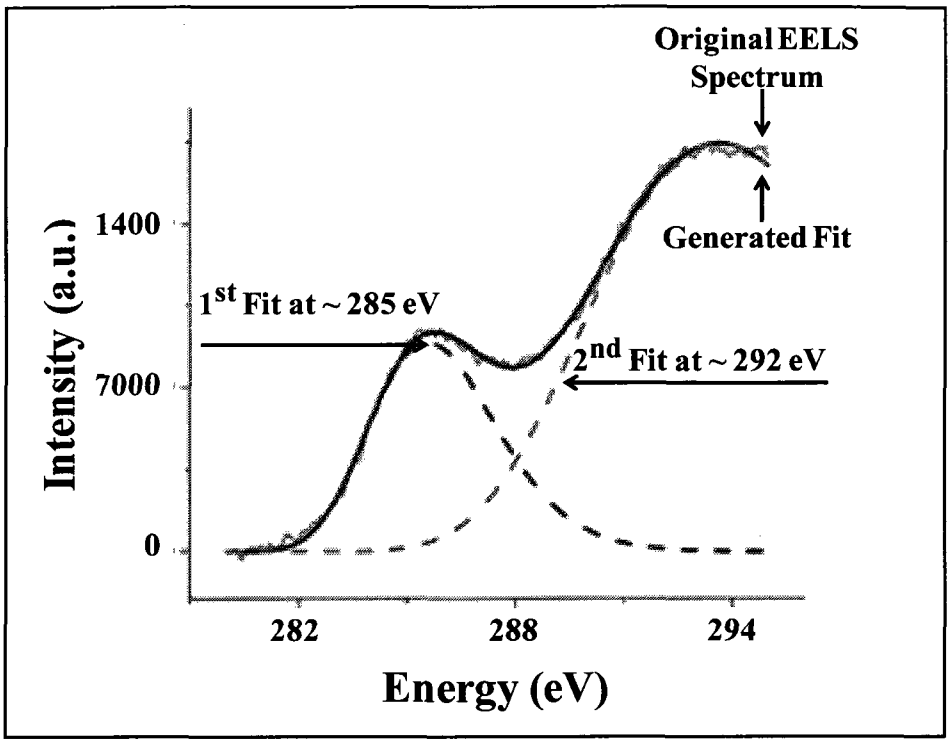

Figure 5.12 Deconvolution of the core loss EELS spectrum of carbon onions, prepared at 1700°C. The original spectrum was deconvolved using 2-peak fit and the asymmetric f-variance function.

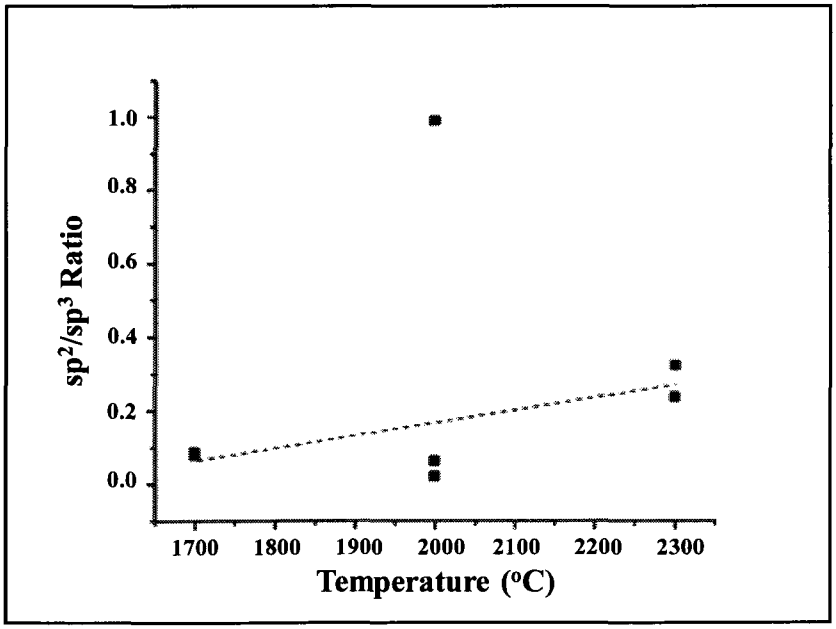

Figure 5.13 A plot showing an increase in the sp^2/sp^3 ratio in carbon onions as a function of synthesis temperature. The results from the 2000°C were variable due to synthesis uniformity issues.

Only carbon onion samples prepared at 2000°C continued to display a wide range of values. Information from a group member[4] who participated in the synthesis experiments indicated that synthesis uniformity issues could be an issue at the 2000°C synthesis temperature.

5.4.1. Investigation of Synthesis Uniformity by SEM

SEM images shown in Figure 5.14 indicated that synthesis uniformity issues may be present. Synthesis was fairly uniform for carbon onions grown at 1700°C. However, carbon onions grown at 2000°C showed evidence of microcrystallite graphite formation in addition to carbon onion synthesis. Carbon onions grown at 2300°C showed better uniformity than those grown at 2000°C but less uniformity than samples grown 1700°C, with some microcrystallite graphite formation observed.

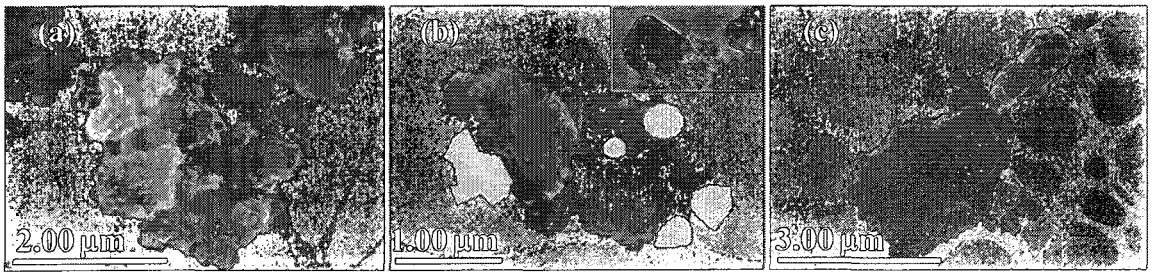

Figure 5.14 SEM surface images of carbon onions synthesized at temperatures (a) 1700°C (b) 2000°C and (c) 2300°C. The inset in (b) is a TEM image. Images by: Raied A. Al-Duhileb.

References

1. R. Egerton, "Chapter 3: Electron Scattering Theory," Electron Energy Loss Spectroscopy in the Electron Microscope (Plenum Press, New York, NY, 1986) pp. 129-228.

2. S. Tomita, T. Sakurai, H. Ohta, M. Fujii, and S. Hayashi, "Structure and electronic properties of carbon onions", The Journal of Chemical Physics **114**: 7477 (2001).

3. J. Titantah, and D. Lamoen, "Technique for the sp^2/sp^3 characterization of carbon materials: Ab initio calculation of near-edge structure in electron-energy-loss spectra", Physical. Review B **70**, 075115 (2004).

4. Benjamin W. Jacobs, Ph.D. during NSF DMI-0631978, IREE: Nano-Mechanical and Electronic Investigations with Tokyo Institute of Technology (2007).

Chapter 6

Conclusion and Future Work

6.1. Discussed Research Conclusion

Qualitative research on the fundamental electronic properties of carbon nano-materials, such as a-C, carbon onions, C_{60}, carbon nanotubes, and other related fullerenes have been widely reported in the literature; however, the fundamental characteristics of these nano-materials have been less quantitatively studied. In this research, we quantitatively investigated the sp^2/sp^3 bond hybridization ratio in different carbon onion samples using EELS due to the anticipated influence of this electronic property on the frictional performance of carbon onions. We also developed a new approach to accurately investigate the sp^2/sp^3 content within a carbon sample. The previous quantitative investigations reported in the literature are based on symmetrical Gaussian or Lorentzian deconvolution functions. In this thesis, EELS spectrums were analyzed using an asymmetric f-variance deconvolution function to reproduce the characteristics of the leading edges.

The quantitative experimental results, analyzed using the asymmetric f-variance deconvolution function, showed a clear increase in the sp^2/sp^3 bond hybridization ratio in carbon onions. Analysis by symmetric Gaussian and Lorentzian deconvolution functions did not reveal clear increasing or decreasing trends.

Carbon onion samples prepared at 2000°C displayed a wide range of values. These were traced to synthesis uniformity issues using TEM, SEM and, as discussed below, micro Raman spectroscopy.

6.2. Continuing Fundamental Studies: Raman Spectroscopy

The bonding nature of carbon onions can be studied using Raman spectroscopy. This technique sets carbon onions into vibrational modes (phonons), which depend on the atomic mass and bond force constants of carbon atoms, using a laser beam (photons). Preliminary investigations, shown in Figure 6.1 and Table 6.1, provided an independent confirmation of the quantitative EELS results. The carbon onion temperature series samples were investigated by room temperature micro Raman spectroscopy at a wavelength of 532 nm. As carbon onions are multi-shell fullerenes, C_{60} was also investigated as a control. A nearly 50% decrease in the FWHM of the *G* peak was observed for carbon onion samples synthesized at 1700°C versus 2300°C. Also, the intensities of both the *D* and *G* peaks were greatly reduced in the 2000°C sample, providing further indication of sample uniformity issues. All three carbon onion samples displayed a broad peak at about 985 cm^{-1}. This is tentatively identified as a disordered amorphous carbon peak. We note that the intensity of this peak was greatly reduced in the 2300°C sample.

These preliminary micro Raman investigations were conducted at room temperature. Low temperature (77K) Raman spectroscopy of multi-walled carbon onions,

which would be resolved into a series of clear peaks, would be very beneficial for examining their vibrational modes in extreme environment and correlating the results with their tribological performance.

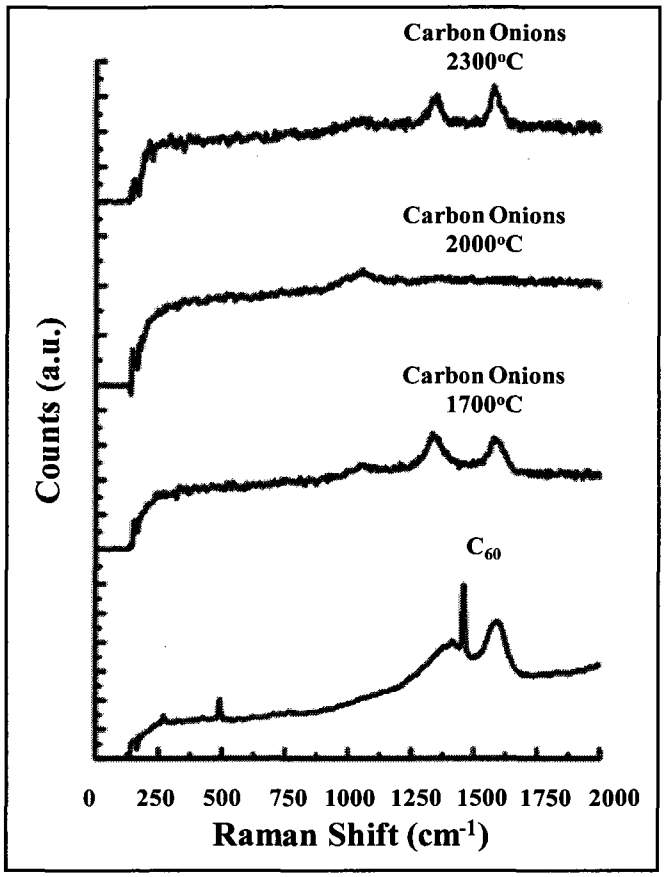

Figure 6.1 Experimental Raman spectra of C_{60} and carbon onion samples prepared at increasing synthesis temperature.

Table 6.1 Raman spectroscopy of C_{60} and carbon onions at wavelength 532 nm.

	C_{60}	CO 1700°C	CO 2000°C	CO 2300°C
Peak (cm^{-1})	271.5			
	492.1			
		991.5	984.6	984.9
		1340.3	1347.2	1348.0
	1368.0			
	1462.7			
		1586.0	1579.2	1579.4
	1593.1			
FWHM (cm^{-1})	45.9			
	16.7			
		1837.4	1720	1592[b]
		46.5	24.1[a]	42.7
	214.8			
	14.9			
		43.1	24.8[a]	21.9
	105.8			
Tentative ID	$H_g(1)$			
	$A_g(1)$			
		-	-	-
		D	D	D
	$H_g(1)+H_g(5)$			
	$A_g(2)$	G	G	G
	$A_g(1)+H_g(5)$			
ID Reference	1	2	2	2

a. Although listed in Table 6.1, the intensities of these two peaks were very weak.
b. The intensity of this peak was very weak.

6.3. Continuing Application Studies: Irradiated Carbon Onions

Carbon onions have demonstrated excellent tribological performance in air and vacuum environments. Lubricants that can function well in a vacuum environment are greatly needed for moving mechanical parts in space, e.g., for solar panel and robotic arm deployment and retraction. In addition to being an extreme vacuum environment, space is a high radiation environment. High radiation environments are also found in other application areas, such as particle colliders and nuclear reactors. Therefore, experimental and theoretical investigations can be conducted to explore the radiation resilience of carbon onions, pending their application in extreme radiation environments including space, which is also a vacuum environment.

Experiments to irradiate carbon onion samples using highly ionized beams are ongoing. The carbon onions are being exposed to heavy ion irradiation at the National Superconducting Cyclotron Laboratory (NSCL) at Michigan State University and their post-radiation properties are being characterized using the quantitative approaches developed in this research. Experiments to date have been performed with primary beams Oxygen-16, Argon-40 and Calcium-48. Irradiations for a cumulative dose of 10,000 Gray (Joule/kg) are performed at 140 MeV/nucleon and 70 MeV/nucleon to test the influence of charge-to-mass ratio on coupling between heavy ion species and carbon onions, while maintaining energy conditions comparable to those encountered in space, nuclear reactors and particle collider environments.

Results to date indicate that carbon onions may respond to heavy ion irradiation with self-healing and self-annealing reactions that are parallel to those observed at increased synthesis temperatures. HRTEM images of pre-radiation carbon onions synthesized at 1700°C are shown in Figure 6.2. The image, shown in (a), displays carbon

onions with typical spherical morphologies, with some defects observable in the atomic planes. The image, shown in (b), displays a feature of two fused onions. This feature could be found at 1700°C but it was rarely observed.

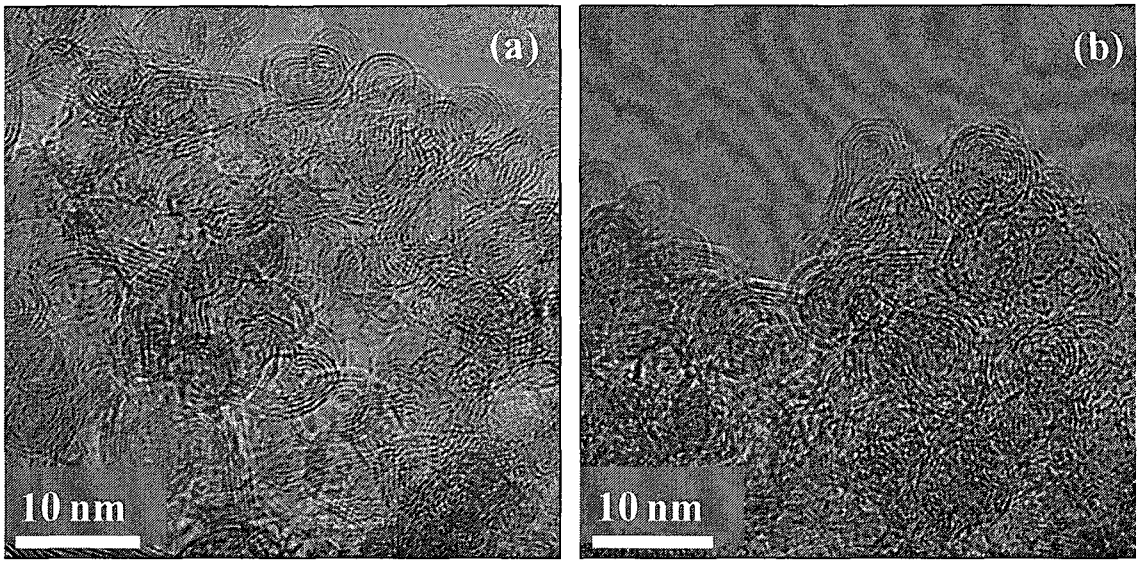

Figure 6.2 HRTEM images of pre-radiation carbon onion samples prepared at1700°C. Typical spherical morphologies are observed in (a). A fused onions feature is observed in (b). Images by: Xudong Fan, with Kaylee McElroy, and Virginia M. Ayres.

HRTEM images of carbon onions synthesized at 1700°C and irradiated with a 10,000 Gray dose of fully stripped Calcium-48 heavy ion are shown in Figure 6.3. We first note that the structural integrity of the carbon onions was largely maintained. The results of irradiation at 70 MeV/nucleon (left hand side) included a greater frequency of fused onions (a), and an increase in the polygonal nature of the atomic layers (b). Areas such as (c) showed some evidence for conversion into another form of carbon such as graphite or amorphous carbon. The results of irradiation at 140 MeV/nucleon (right hand side) showed a similar increase infused and polygonal onions (d and e) but also showed

more evidence of defective atomic planes in both. Furthermore, evidence for conversion of carbon onions into defective amorphous carbon in local areas was clearly observed (f). When these results and other are quantified using the methods developed in this research, it will provide a quantitative description of energy deposition in the carbon onion system during irradiation by heavy ions.

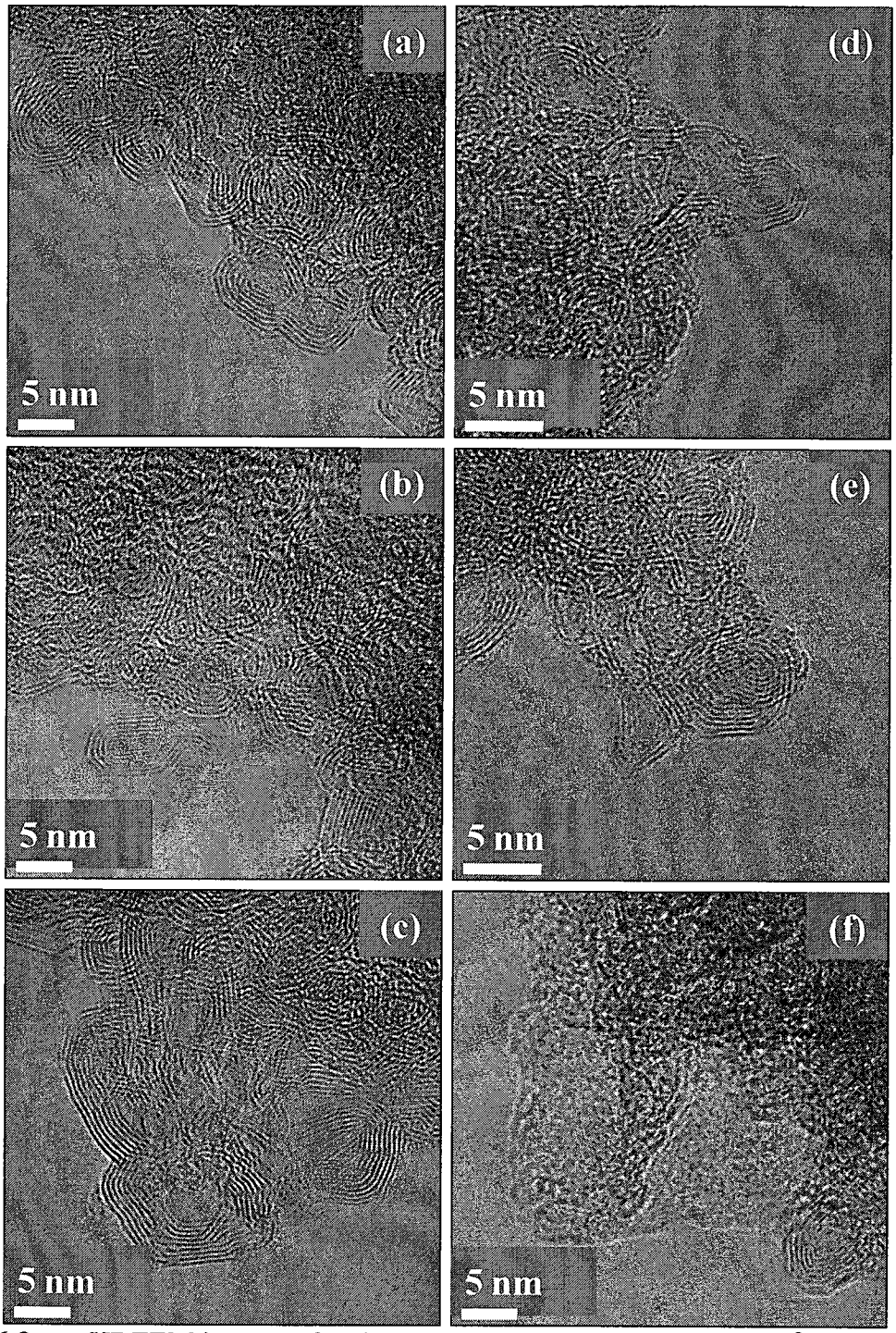

Figure6.3 HRTEM images of carbon onion samples prepared at 1700°C following irradiation with fully stripped Calcium-48 heavy ions at energies (a-c) 70 MeV/nucleon and (d-e) 140 MeV/nucleon. Images by: Xudong Fan, with Kaylee McElroy, and Virginia M. Ayres.

6.4. Continuing Application Studies: Tribological Performance of Carbon Onions in Harsh Environments

To eliminate the frequent operational failures and serious incidents associated with the performance of the conventional lubricant approaches, new nano-particle solid based lubricants are currently under investigation for use in both ordinary and harsh environments. Nano-particulate molybdenum and tungsten disulfides have been successfully used for improving the frictional performance of these nano-particle solid based lubricants in terrestrial applications; however, the environmental impact of nano-sized heavy metal derivatives is still under investigation. Nano-carbon materials such as carbon onions, carbon nanotubes, C_{60}, and related fullerenes are also under investigation as environmentally benign alternatives. The best overall lubrication performance across air, vacuum and polymer environments to date has been achieved with carbon onions[3].

Although preliminary tribological studies of carbon onions showed an improved frictional performance in air and vacuum, further investigations are desired to examine their frictional behavior in harsh environments seen in terrestrial industries and space. In addition, future experimental investigations should consider assessing the tribological performance of different carbon onion samples prepared at increasing annealing temperatures, and studying the effects on their outer structures post performing the frictional assessment experiments.

References

1. Z. Dong, P. Zhou, J. Holden, P. Eklund, M. Dresselhaus, and G. Dresselhaus, "Observation of higher-order Raman modes in C_{60} films", Physical Review B **48**: 2862–2865 (1993).

2. S. Tomita, T. Sakurai, H. Ohta, M. Fujii, and S. Hayashi, "Structure and electronic properties of carbon onions", The Journal of Chemical Physics **114**: 7477 (2001).

3. A. Hirata, M. Igarashi, and T. Kaito "Study on solid lubricant properties of carbon onions produced by heat treatment of diamond clusters or particles", Tribology International **37**: 899–905 (2004).